

TanDEM-X multiparametric data features in sea ice classification over the Baltic sea

Marjan Marbouti, Oleg Antropov, Jaan Praks, Patrick B. Eriksson, Vahid Arabzadeh, Eero Rinne & Matti Leppäranta

To cite this article: Marjan Marbouti, Oleg Antropov, Jaan Praks, Patrick B. Eriksson, Vahid Arabzadeh, Eero Rinne & Matti Leppäranta (2021) TanDEM-X multiparametric data features in sea ice classification over the Baltic sea, *Geo-spatial Information Science*, 24:2, 313-332, DOI: [10.1080/10095020.2020.1845574](https://doi.org/10.1080/10095020.2020.1845574)

To link to this article: <https://doi.org/10.1080/10095020.2020.1845574>



© 2020 Wuhan University. Published by Informa UK Limited, trading as Taylor & Francis Group.



Published online: 07 Dec 2020.



Submit your article to this journal [↗](#)



Article views: 551






View related articles [↗](#)



View Crossmark data [↗](#)

TanDEM-X multiparametric data features in sea ice classification over the Baltic sea

Marjan Marbouti ^a, Oleg Antropov ^b, Jaan Praks^c, Patrick B. Eriksson^d, Vahid Arabzadeh^e, Eero Rinne^d and Matti Leppäranta ^a

^aInstitute for Atmospheric and Earth System Research / Physics, Faculty of Science, University of Helsinki, Helsinki, Finland; ^bVTT Technical Research Centre of Finland, Espoo, Finland; ^cAalto University, Department of Electronics and Nanoengineering, Espoo, Finland; ^dFinnish Meteorological Institute, Helsinki, Finland; ^eAalto University, Department of Applied Physics, New Energy Technologies Group, Espoo, Finland

ABSTRACT

In this study, we assess the potential of X-band Interferometric Synthetic Aperture Radar imagery for automated classification of sea ice over the Baltic Sea. A bistatic SAR scene acquired by the TanDEM-X mission over the Bothnian Bay in March of 2012 was used in the analysis. Backscatter intensity, interferometric coherence magnitude, and interferometric phase have been used as informative features in several classification experiments. Various combinations of classification features were evaluated using Maximum likelihood (ML), Random Forests (RF) and Support Vector Machine (SVM) classifiers to achieve the best possible discrimination between open water and several sea ice types (undeformed ice, ridged ice, moderately deformed ice, brash ice, thick level ice, and new ice). Adding interferometric phase and coherence-magnitude to backscatter-intensity resulted in improved overall classification performance compared to using only backscatter-intensity. The RF algorithm appeared to be slightly superior to SVM and ML due to higher overall accuracies, however, at the expense of somewhat longer processing time. The best overall accuracy (OA) for three methodologies were achieved using combination of all tested features were 71.56, 72.93, and 72.91% for ML, RF and SVM classifiers, respectively. Compared to OAs of 62.28, 66.51, and 63.05% using only backscatter intensity, this indicates strong benefit of SAR interferometry in discriminating different types of sea ice. In contrast to several earlier studies, we were particularly able to successfully discriminate open water and new ice classes.

ARTICLE HISTORY

Received 4 February 2020
Accepted 29 October 2020

KEYWORDS

Sea ice classification;
Random Forests (RF);
Maximum Likelihood (ML);
Support Vector Machine (SVM); backscatter;
coherence; sar
interferometry; Synthetic
Aperture Radar (SAR)

1. Introduction

Synthetic Aperture Radar (SAR) data have been used to monitor ice-covered maritime regions for approximately three decades (Ressel, Frost, and Lehner 2015). Satellite SAR imaging capability is independent of cloud coverage and light conditions and allows to cover the entire Earth within short periods of time in contrast to airborne and shipborne data (Ressel, Frost, and Lehner 2015; Ressel and Singha 2016; Sandven and Johannessen 1989; Ressel et al. 2016; Park et al. 2016; Liu, Guo, and Zhang 2018; Liu, Li, and Guo 2017). SAR missions operating at various wavelengths have been used for sea ice research in Arctic and Antarctic regions for several decades. Studied sea ice properties included ice drift (Leppäranta, Sun, and Haapala 1998; Hamidi et al. 2011; Karvonen 2012; Kwok, Spreen, and Pang 2013), sea state and wave propagation into sea ice (Liu, Holt, and Vachon 1991; Vachon et al. 2004), ice concentration, iceberg detection (Dierking and Wesche 2014), and ice-type classification (Dierking and Wesche 2014; Soh and Tsatsoulis 1999; Soh et al. 2004; Bogdanov et al. 2005; Breivik, Eastwood, and

Lavergne 2012; Zakhvatkina et al. 2013; Clausi and Zhao 2002, 2003; Clausi and Yue 2004; Ochilov and Clausi 2012; Dierking and Pedersen 2012; Scheuchl, Caves, Cumming, and Staples 2001; Scheuchl, Hajnsek, and Cumming 2003; Karvonen 2004; Similä et al. 2001). Respective missions include Radar Satellite-1 (RADARSAT-1), RADARSAT-2, European Remote Sensing satellites (ERS-1 and ERS-2), and Environmental Satellite (EnviSat) acquiring images at C-band. Constellation of Small Satellites for Mediterranean basin Observation (Cosmo-SkyMed) and TerraSAR-X/TanDEM-X have acquired X-band imagery, and Advanced Land Observation Satellite (ALOS) Phased Array type L-band Synthetic Aperture Radar (PALSAR) has provided L-band radar imagery for sea ice research (Rigor and Wallace 2004; Maslanik et al. 2007; Stroeve et al. 2007; Scheuchl et al. 2004; Askne, Leppäranta, and Thompson 1992).

In the Baltic Sea, winter navigation is the main motivation for the ice classification research. This study concentrates on the Baltic Sea where ice conditions during winter hinder marine navigation. Baltic

Sea is a brackish water basin and its ice is structurally similar to polar first-year sea ice but has much lower salinity. For safe navigation, icebreakers and commercial vessels require accurate ice condition information to select optimal routes and assess the need for icebreaker assistance. To aid navigation and safe shipping, the Finnish Meteorological Institute (FMI) provides daily ice charts. For this service, FMI uses mainly C-band SAR satellite images, particularly from RADARSAT-2 and Sentinel-1 missions (Gegiuc et al. 2017). These sensors have sufficient resolution (100 m) for general navigation needs. However, in order to distinguish ice ridges, heavily deformed ice and new ice formation in more details and get better understanding about mechanisms of sea ice formation, sensors with higher spatial resolution should be used, e.g. operating at X-band. Another advantage of X-band SAR over C-band is its higher sensitivity in assessment of sea ice surface properties, small-scale surface roughness and sea ice inclusions due to shorter wavelength (Ressel, Frost, and Lehner 2015; Dierking 2013; Fors 2016). Currently, the FMI service uses trained experts for sea ice classification and ice chart production. This is time consuming and expensive. Furthermore, the same SAR data interpreted by different experts can, and often does, lead to somewhat different results. In view of increased data volumes from operational and planned X-band sensors (e.g., ICEYE constellation), a need for automated classification procedure is getting stronger. This would if not replace manual expert interpretation, but at least provide valuable pre-classification to the analysis. To date, the potential of automated sea ice classification was demonstrated in several studies using backscatter intensity data (Clausi and Zhao 2003; Gegiuc et al. 2017; Sandven et al. 2012; Barber and LeDrew 1991; Clausi 2001; Shokr 2009). However, no feasible operational algorithm exists. Since different ice types can have similar backscatter-intensity, a single image feature can be inadequate for sea ice classification (Ressel, Frost, and Lehner 2015; Karvonen 2004). Several earlier studies (Mäkynen and Hallikainen 2004; Dierking 2010) concluded that using only backscatter-intensity data is not sufficient to delineate different ice types reliably. There is an evidence (Dierking 2010) that additional image layers including higher order textural features are necessary and a large feature space has to be generated in order to train a classifier successfully. Among suitable techniques for describing the image texture, Gray-Level Co-occurrence Matrix (GLCM) features have been tested in sea ice classification recently (Ressel, Frost, and Lehner 2015).

Several studies focusing on InSAR signatures of sea ice (Dammert, Leppäranta, and Askne 1998; Berg, Dammert, and Eriksson 2015; Marbouti et al. 2017; Dierking, Lang, and Busche 2017;

Laanemäe, Uiboupin, and Rikka 2016) have demonstrated that coherence-magnitude and InSAR-phase provide valuable information about the sea-ice dynamics. Dammert, Leppäranta, and Askne (1998) found several relationships between backscatter-intensity and coherence-magnitude features over low-salinity ice, further expanded by Berg, Dammert, and Eriksson (2015). Marbouti et al. (2017) used backscatter-intensity and InSAR-phase features for finding sea ice displacement over fast ice. Dierking, Lang, and Busche (2017) used InSAR-phase feature for retrieving the ice surface topography. Laanemäe, Uiboupin, and Rikka (2016) used backscatter-intensity and coherence-magnitude features for sea ice classification. This motivates to study connections between backscatter-intensity, InSAR coherence-magnitude, and InSAR-phase, as well as the benefit of interferometry compared to backscatter, also in the sea-ice classification context.

In this study, we aim to extend the classification parameter space by introducing SAR interferometry and investigate the applicability of coherence-magnitude and InSAR-phase to improve automated sea ice classification at X-band. Specific goal is to establish a workflow for automated classification, using X-band interferometric SAR data acquired by the TanDEM-X mission, with preliminary results shortly communicated in Marbouti et al. (2018).

To date, there was only one study based on TanDEM-X imagery using both backscatter-intensity and coherence-magnitude features for automated sea ice classification (Laanemäe, Uiboupin, and Rikka 2016). Their method was applied over few types of ice: landfast ice, thin smooth ice, pancake ice and open water. Our aim is to increase the number of classified sea ice types, by using more features. Moreover, different sea ice classification algorithms are evaluated and compared here to select the best performing algorithm along with best combination of used image features.

The study concentrates on evaluating the added value of SAR interferometry versus the use of backscatter intensity on sea-ice classification, and compares three popular classification approaches (RF, ML, and SVM classifiers) for differentiating between open water and various sea ice types (undeformed ice, ridged ice, moderately deformed ice, brash ice, thick level ice, new ice).

The particular objectives of this study are:

(i) to assess the potential of various SAR features, such as backscatter-intensity, interferometric coherence-magnitude and interferometric phase, as well as their combinations, for characterizing sea ice using X-band SAR data and,

(ii) to determine which classification method (RF, ML, SVM) is more suitable for inferring sea ice types using studied InSAR features.

The article is organized as follows. We describe our study site, SAR data, relevant theoretical information and processing methodologies in Section 2. Classification results are provided in Section 3. Relative performance of different SAR features, comparison between RF, ML, and SVM algorithms, classification performance for different features, effects of image acquisition geometry on ice type classification, as well as comparison with prior works are given in Section 4. Finally, Section 5 summarizes the paper with conclusions, potential for future research and application of the demonstrated classification approaches.

2. Materials and methods

2.1. Study area

Our study area (Marbouti et al. 2018) is located in the vicinity of Hailuoto Island in the north of the Baltic Sea (Figure 1a). The Baltic Sea is a semi-enclosed brackish sea in northern Europe. Sea ice starts to form in November and its maximum extent is reached between January and March (Seinä and Peltola 1991). Sea ice breakup starts in April and typically completes by the beginning of June. The maximum annual ice coverage over the Baltic Sea is from 12% to 100% and its average is about 40% (Seinä and Palosuo 1996).

The sea ice cover in the Baltic Sea can be divided into landfast ice and drift ice. Landfast ice is fastened to the coastline and islands, while further offshore drift ice is moving along by winds and sea currents. The mean thickness of thermodynamically grown ice is 70 cm with inter annual range of 50–120 cm (Palosuo, Leppäranta, and Seinä 1982). Thermally grown sea ice consists mainly of congelation ice and snow-ice, and its salinity is less than two per mill

(Leppäranta and Myrberg 2009). The thickness of ice ridges is typically 5 to 15 m (Leppäranta and Hakala 1992).

For this study, we have acquired TanDEM-X image over the Baltic Sea on March 30, 2012 (Figure 1a). This was a mild winter but the northern and eastern basins of the Baltic Sea froze over. At the end of March, the ice in the Bay of Bothnia was tightly packed into the northeast part (Figure 1b), the InSAR data covered very close drift ice and landfast ice. In the area of the frame, the thickness of landfast ice was mostly 35–60 cm, and the drift ice largely contained deformed ice. This chart is not detailed enough for our study, and therefore an independent high-resolution reference ice chart was prepared in FMI Ice Service based on operational satellite data and ground truth from icebreakers and fixed observation sites.

The ice types chosen for the study contain six categories with different degrees of thickness and surface roughness, and open water (Table 1). These ice types can be identified by the FMI Ice Service in the operational ice charting that is based on the World Meteorological Organization (WMO) sea ice nomenclature. The categories or their symbology are included in the operational ice charting and are essential to icebreaking and navigation operations.

Landfast ice is a particular ice type that covers a large portion of the analyzed image but was left outside the classification. Landfast ice is a kinematic concept, defined on the basis of immobility. The boundary of landfast ice and drift ice is dynamic, where fractures form depending on the thickness of ice and consolidation between ice floes (Goldstein, Osipenko, and Leppäranta 2009). Thus, landfast ice cannot in general be distinguished from one image. As a matter of fact, our results show clearly how

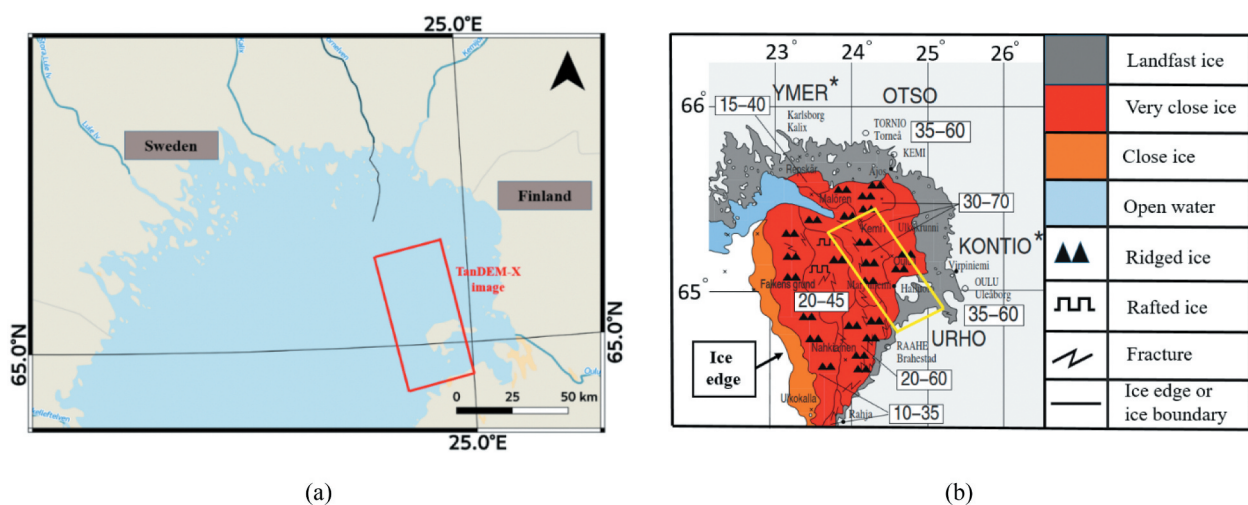


Figure 1. (a) an overview of the Bay of Bothnia, the Baltic Sea with TanDEM-X image footprint shown with red rectangle. The image was acquired on 30 March 2012. (b) Ice chart over the Bay of Bothnia on 30 March 2012. The yellow rectangle shows the TanDEM-X footprint.

Table 1. Description of sea ice classes.

Ice type	Definition
Open water	A sea surface which is free of ice but may contain some ice fragments, by definition covering less than 1/10 of the surface.
New ice	New ice represents all forms of thin newly formed ice from frazil ice with almost liquid-like attributes to a uniform crust of up to 5 cm in thickness.
Undeformed Ice	Ice thicker than 10 cm, not significantly deformed but including rough surface properties.
Thick Level Ice	Ice thicker than 10 cm with a smooth surface and without any deformation. The ice surface might have been refrozen from flooded water or melted snow.
Ridged ice	Ice thicker than 10 cm with frequent occurrences of deformed ice, both rafted and ridged. Most of this ice type has been broken and piled to pressure ridges by compressive forcing. In this ice type, there is typically a network of ridge lines crisscrossing in a sheet of otherwise level first-year ice but also heavily deformed ice with virtually no level ice present.
Moderately deformed ice	Drift ice thicker than 10 cm, including a mixture of different ice types. The field consists of originally broken drift ice of different stages of development, including both rafted and ridged ice but also patches of level ice.
Brash ice	Ice broken into a fairly homogenous surface of very small ice blocks and typically identified by a high backscatter coefficient. In the scenes studied in this paper, brash ice can mainly be identified along known, fixed shipping lanes. It was chosen into the categorization because of its distinct features and evident detectability. Brash ice also forms at ice edges, broken and compacted by wind and waves into wide and thick zones and causing considerable harm to navigation.

fracturing processes have caused mixing between landfast ice and drift ice with time, and therefore landfast needs to be studied from sequential image data (Marbouti et al. 2017).

2.2. SAR data description

2.2.1. InSAR theory in the context of the study

The interferometric coherence between two complex SAR images S_1 and S_2 represents the complex cross-correlation between them:

$$\gamma = \frac{\langle s_1 s_2^* \rangle}{\sqrt{\langle s_1 s_1^* \rangle \langle s_2 s_2^* \rangle}}, 0 \leq |\gamma| \leq 1 \quad (1)$$

where asterisk denotes complex conjugation. The coherence is used as an indicator of the quality of the interferogram (Hurtado 2012). Interferometric phase $\varphi = \arg(\gamma)$ gives information about the path difference between the different antenna positions and the target and can be used for topographic measurement provided SAR images were acquired at slightly different incidence angles (Plank 2014). The SAR system measures the interferometric phase difference φ related to the path length difference as:

$$\varphi = \frac{2\pi a}{\lambda} dR = -\frac{2\pi a}{\lambda} \sin(\theta - \alpha) \quad (2)$$

where λ is the SAR wavelength, R is satellite to target distance, dR is the path length difference between the two antennas, B is the perpendicular baseline, θ is the incidence angle, and α is the baseline tilt angle with respect to the horizontal, and the parameter a takes value of 1 or 2 for single-pass or multi-pass case, respectively. In this study, aa value is equal to one (Plank 2014).

2.2.2. TanDEM-X image selection and preprocessing

TanDEM-X Coregistered Single Look Slant Range Complex (CoSSC) products were used in the study. The image was acquired on March 30, 2012 in the stripmap mode in bistatic InSAR configuration, at HH polarization.

Bistatic formation allows to avoid temporal decorrelation, with TanDEM-X being presently the only available bistatic spaceborne SAR mission. Its relatively short along track baseline and big perpendicular baseline is useful for ice mapping (Dierking, Lang, and Busche 2017). Also, X-band SAR compared to C-band has higher sensitivity toward surface structures (Ressel, Frost, and Lehner 2015; Dierking 2013). On the other hand, keeping in mind limited availability of such data to operational end-users, little research on sea ice classification using X-band InSAR data has been performed so far (Laanemäe, Uiboupin, and Rikka 2016).

In this study, we screened imaging data between 2010 and 2019 acquired using standard bistatic imaging mode. The project concentrated on Baltic Sea, thus we tried to choose images where sea ice is nearly stable and no melting is happening, limiting available scenes to those acquired in March. On the other hand, the most suitable TanDEM-X data for inferring sea ice topography is TanDEM-X Science Phase, which started in September 2014 and lasted for 17 months (Maurer et al. 2016). The Science Phase was initiated to demonstrate new products and applications such as digital elevation models with higher accuracies than in standard mode or measurements of ocean currents. The comparatively large baselines in this phase translated to a very high sensitivity for object elevations on the order of decimeters. However, unfortunately, we did not find any option of science phase over Baltic Sea during September 2014 to February 2016 (science phase period); that's why the choice was made to rely on standard operation mode that leads to somewhat lower topographic mapping accuracy compared to science phase. Image parameters of studied CoSSC scene are collected in Table 2.

Figure 2 shows features of The TanDEM-X image: backscatter-intensity (Figure 2a), InSAR coherence-magnitude (Figure 2b) and InSAR-

Table 2. TanDEM-X image parameters.

Acquisition date	30 March 2012
Acquisition start time	15:55:37
Mode	Stripmap
Polarization	HH
Orbit cycle	167
Relative orbit	24
Effective baseline (m)	240.38
Resolution (m)	2.51
Height of ambiguity (m)	-30.84
Average coherence	0.81
Incidence angle	43.41 deg

phase (Figure 2c). TanDEM-X data were orthorectified using ESA SNAP software. TanDEM-X InSAR-phase ramp was compensated to remove its effect on the classification performance (Sadeghi et al. 2014; Solberg et al. 2013; Solberg, Weydahl, and Astrup 2015; Marbouti et al. 2020). All features were additionally filtered using (7×7) boxcar filter. Land area was removed by applying land masking. Finally, linear stretching to dynamic range [0;255] was applied over each feature before running classification experiments.

2.3. Reference classification map

Sea ice charts for the Bay of Bothnia are routinely produced by the FMI experts. The ice charts provide a daily source of information on the ice conditions. Experts delineate ice chart polygons assigning to the specific ice types. The charts are based on visual interpretation of SAR imagery as the principal source of information. Currently, mainly RADARSAT-2 and Sentinel-1 SAR imagery with wide swaths are used (Gegiuc et al. 2017); however, X-band SAR sensors such as Cosmo-SkyMed and TerraSAR-X with narrower swaths are also deemed useful. The experts also use visible and thermal infrared imagery from Moderate Resolution Imaging Spectroradiometer (MODIS), in-situ observations, sea ice reports from icebreakers, and sea ice models in the production of the ice charts.

In this study, a sea ice expert produced a reference map by manually classifying sea ice based on the TanDEM-X features. The reference map in this study (ice chart shown in Figure 3) is in fact considerably

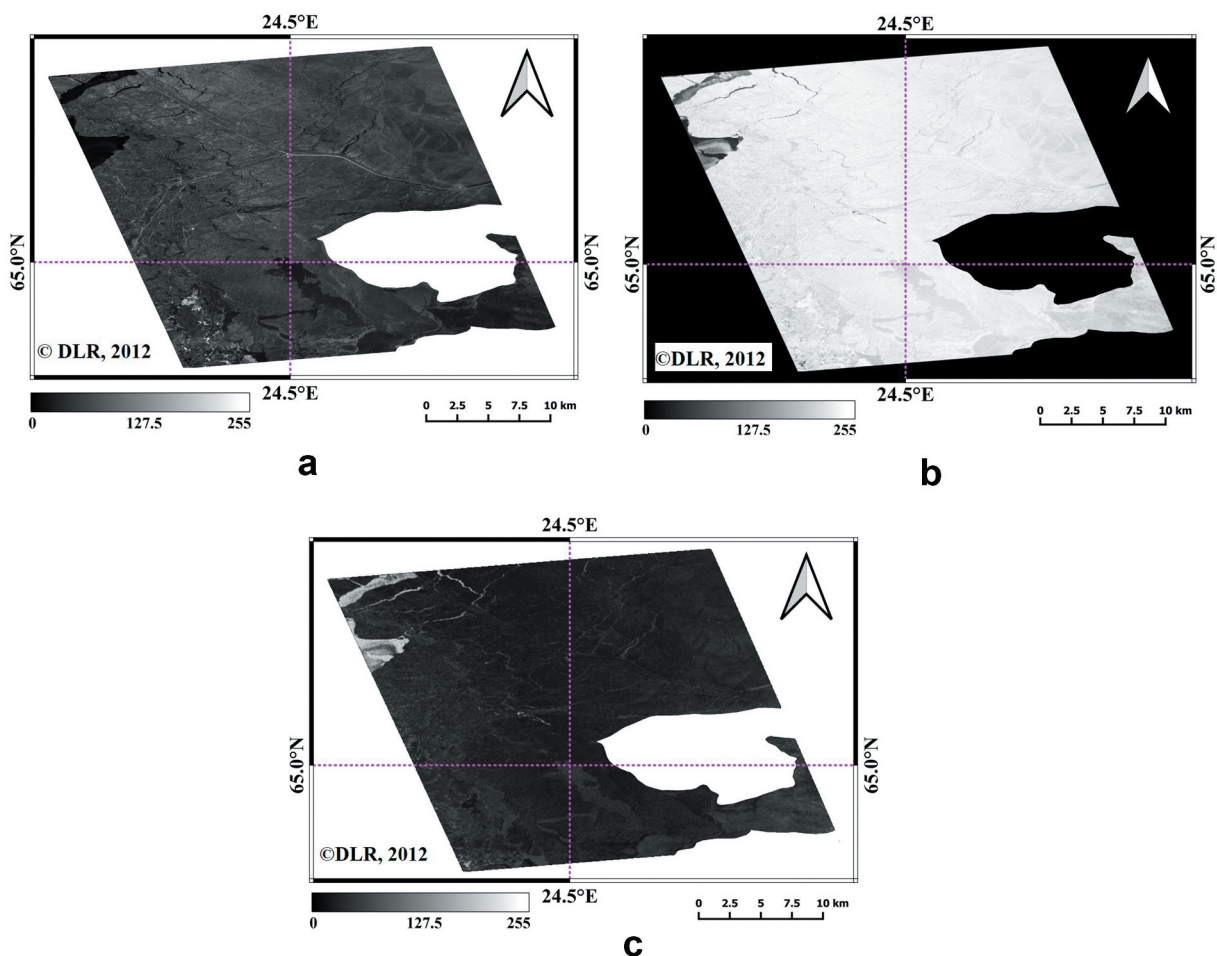


Figure 2. TanDEM-X image features: (a) backscatter intensity; (b) coherence-magnitude; (c) InSAR-phase. The image was acquired 30 March 2012. Land mask was applied. The features were linearly stretched to [0;255] dynamic range.

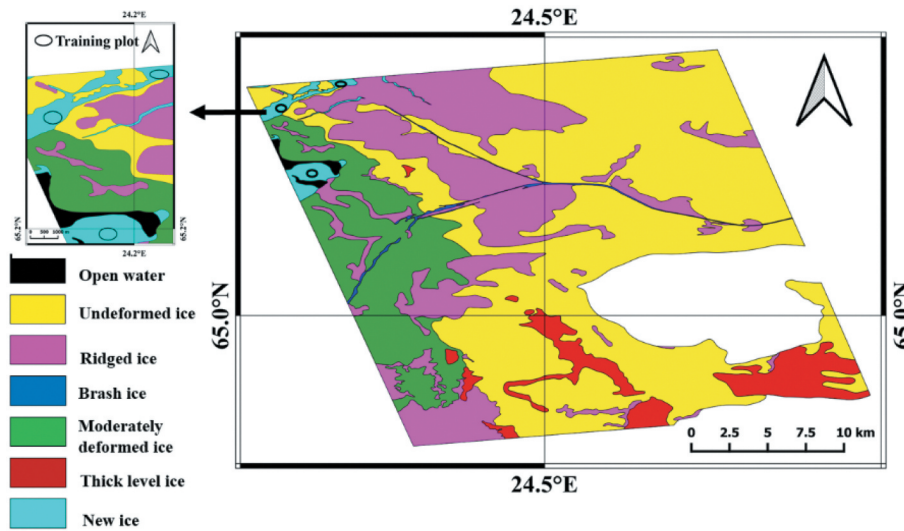


Figure 3. Reference classification map for 30 March 2012. New ice class with training plots are shown in the upper left corner of the image.

more detailed than routine daily ice charts to respond to the high resolution of the source data.

2.4. Proposed classification approach

To improve classification performance, careful selection of representative training data is critical (Antropov et al. 2014). Image area was almost 3558 km². A total of 14,000 pixels (2000 pixels per each class) were randomly selected based on feature properties by the sea ice expert.

RF and ML classification has been done using ESA Sentinel Application Platform (SNAP) software. SVM

classifier was implemented using MATLAB software. In order to evaluate the added value of InSAR features compared to backscatter intensity, several classification experiments were performed: separately for each TanDEM-X feature, for their various combinations, as well as all features combined together.

After classification processes (Sections 2.5 and 2.6 and 2.7), each pixel was assigned to a sea ice type and open water. Majority voting (5 * 5 neighborhood) was applied over classification maps to achieve more homogeneous areas. Figure 4 shows the workflow of our proposed algorithm for open water and sea ice-type classification.

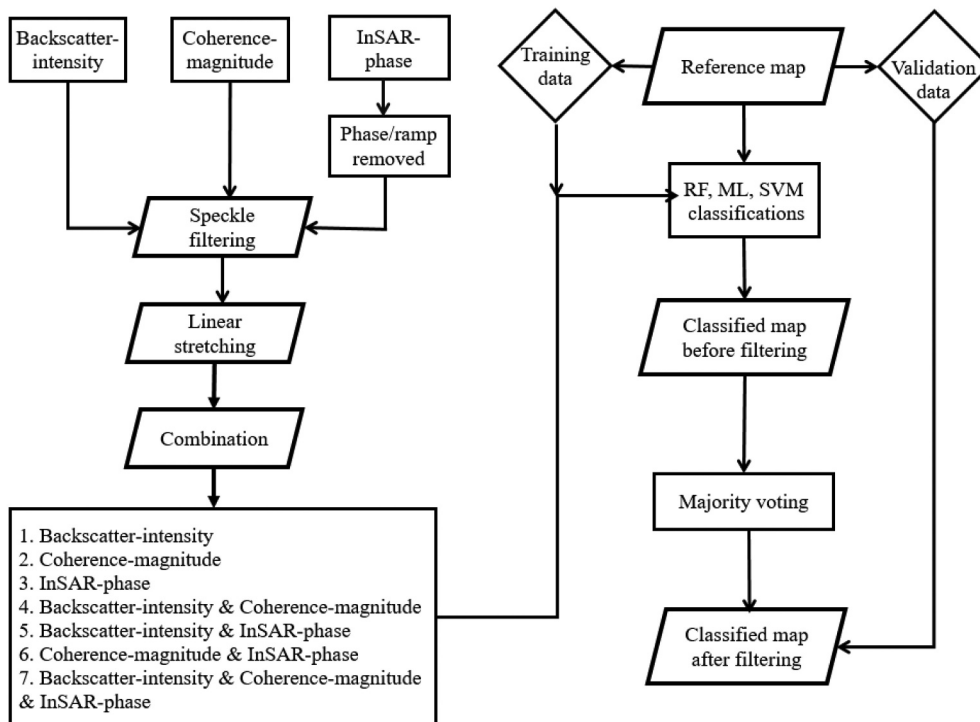


Figure 4. Flowchart of the proposed approach for open water and sea ice-type classification.

2.5. RF classification

RF is a classification and regression tree technique invented by Breiman (2001). Breiman (2001) defined an RF as a classifier consisting of a collection of tree-structured classifiers $\{t(x, \Theta_k), k = 1, \dots\}$ where the $\{\Theta_k\}$ are independent identically distributed random vectors and each tree casts a unit vote for the most popular class at input x (Breiman 2001).

RF lets each tree vote for the class membership, and assigning the respective class according to the majority of the votes that result in taking advantage of the high variance among individual trees (Stumpf and Kerle 2011). RF has proven its power in handling classification with a big data of high dimensional feature spaces. These RF properties prove robust and accurate performance on complex datasets (Du et al. 2015).

SNAP software includes an application to perform RF pixel-based image classification. The SNAP allows us to train a classifier using various features and training vector data, with the resulting classifier model saved as a model file. The training vector data must contain polygons with a positive integer field representing the class label. In the next step, the image classification by using the provided model file is performed on corresponding features, with each pixel assigned a class label. In this study, number of training samples and trees in the forest were 14,000 and 100, respectively. Based on Oshiro's study (Oshiro, Perez, and Baranauskas 2012), the best optimal number for trees are between 64 and 128 trees because increasing the number of trees would bring no significant performance gain, and would only increase the computational cost. Although we tried to use of 10, 50, 100, and 150 trees in this study but the best result were achieved when we used 100 trees and increasing number of tree did not make sufficient change in our result.

2.6. ML classification

ML is a supervised classification approach. That is the procedure of finding the value of one or more parameters for a given statistic which makes the known likelihood distribution a maximum. It is derived from the Bayes theorem, which states that the posteriori distribution $P(w|k)$, i.e., the probability that a pixel with feature vector ' w ' belongs to class ' k ':

$$P(k|w) = \frac{P(k)P(w|k)}{P(w)} \quad (3)$$

where $P(w|k)$ is the likelihood function, $P(k)$ is a priori information, and $P(w)$ is the probability that ' w ' is observed, it is given by:

$$P(w) = \sum_{k=1}^N P(w|k)P(k) \quad (4)$$

where N is the number of classes. $P(w)$ is often behaved as a normalization constant to certify $\sum_{k=1}^N P(k|w)$ sums to 1. Pixel ' x ' is assigned to class ' k ' by:

$$X \in k \text{ if } P(k|w) > P(j|w) \text{ for all } j \neq k \quad (5)$$

ML often assumes that the distribution of the data within a given class ' k ' obeys a multivariate Gaussian distribution. It is then convenient to define the log likelihood:

$$\begin{aligned} g_k(w) &= \ln P(w|k) \\ &= \frac{1}{2} (w - \mu_k)^t C_k^{-1} (w - \mu_k) - \frac{N}{2} \ln(2\pi) \\ &\quad - \frac{1}{2} \ln(|C_k|) \end{aligned} \quad (6)$$

Since log is a monotonic function, Equation (5) is equivalent to:

$$X \in k \text{ if } g_k(w) > g_j(w) \text{ for all } j \neq k \quad (7)$$

Each pixel is assigned to the class with the highest likelihood (Ahmad and Quegan 2012). The SNAP was used to perform supervised ML pixel-based image classification. Within ML classifier, we do not have any parameter to change except the number of training samples; it has been set to 14,000 similar to RF classifier to enable fair comparison of their performance.

2.7. SVM classification

SVMs have their roots in Statistical Learning Theory (Vapnik 1995). They have been vastly applied to machine vision fields including character, text recognition, and handwriting digit (Vapnik 1995; Joachims 1998). In nowadays, SVMs also are applied to satellite image classification (Huang, Davis, and Townshed 2002; Anthony, Greg, and Tshilidzi 2007). The objective of the support vector machine algorithm is to find a hyperplane in a high-dimensional space that separately classifies the data points. This translates to finding a hyperplane that gives the largest minimum distance to the training examples. The trade-off between minimizing the training error and the complexity of the decision function is controlled by a kernel and kernel parameters (Friedrichs and Igel 2005; Laanemäe 2017). The basic SVM is directly applicable for solving two-class (binary) classification. For multiclass problems such as sea ice classification in this study, the implementation of SVM is approached by multiclass strategy. Two of the common methods to enable this adaptation include the One-Versus -One (OVO) and One-Versus-All (OVA) techniques (Anthony, Greg, and Tshilidzi 2007; Han et al. 2015). The OVA approach represents the earliest and the most common SVM multiclass approach (Melgani

and Bruzzone 2004) and involves the division of a K class dataset into K two-class cases. The OVO approach on the other hand; involves constructing a machine for each pair of classes resulting in K (K-1)/2 machines. Further, majority voting is used to assign a label to current pixel. It is further modified to introduce weighting to the voting process (Anthony, Greg, and Tshilidzi 2007).

In this paper, an error-correcting output codes (ECOC) multiclass model based on SVM binary learners is trained using Matlab environment. Particularly, the OVO approach with K binary learners is used. Number of binary learners is depended on number of classes which exist in data. In this work, there are seven classes, thus the OVO model has 21 binary learners. For training the model, we used 2000 pixels for each classes and total pixels are 14,000, similarly to other experiments.

2.8. Accuracy assessment

Classification performance was evaluated using stratified random sampling approach, in order to have the same number of pixels for each class in the accuracy assessment. Confusion matrix (CM) was calculated for all ice classes, and following accuracy measures were used: Overall Accuracy (OA), User Accuracy (UA), Producer Accuracy (PA), and Kappa coefficient of determination.

$$OA = \frac{\text{Number of correct pixels}}{\text{Total number of pixels}} \quad (8)$$

$$UA = \frac{\text{Number of correctly identified pixels in a given map class}}{\text{Number of pixels claimed to be in that map class}} \quad (9)$$

$$PA = \frac{\text{Number of correctly identified pixels in reference plots of a given map class}}{\text{Number of pixels claimed to be in that map class}} \quad (10)$$

$$Kappa = \frac{\text{Observed accuracy} - \text{chance agreement}}{1 - \text{chance agreement}} \quad (11)$$

3. Results

3.1. Classifications accuracy assessment

Altogether, 14 CMs were calculated for seven types of single and combinations of features in several classification experiments. All experiments are listed in Table 3. Values of OA, UA and PA assessments for all experiments are shown alongside CMs. The best results from 14 experiments (RF, ML and SVM) are presented in Figure 5(a, b). The highest OA in RF, ML, and SVM experiments were 72.93, 71.56, and 72.91% (all three features combined). This suggests that features combination are better than single features for sea ice classification. Table 3 shows the OA with Kappa coefficients statistics gathered for all 14 classification experiments.

3.2. Classification output maps

As it was shown in the previous section, the highest OAs were obtained using combination of all features (backscatter-intensity, coherence-magnitude, and InSAR-phase) with three classifiers. They were 72.93, 71.56, and 72.91% for RF, ML, and SVM, respectively. Figure 6(a, b, c) shows the final classification maps, produced at 10-m spatial resolution, and give a representative overview of the spatial distribution of sea ice classes in the study area.

4. Discussion

4.1. Relative performance of different SAR features

In order to investigate the suitability of different input features and their combinations for the classification

of open water and sea ice types, the accuracy assessment of classification maps produced using various combinations of features was performed.

Table 3. RF, ML, and SVM overall accuracies (OAs) and Kappa coefficients.

Classification features	OA (RF) (%)	Kappa (RF) (%)	OA (ML) (%)	Kappa (ML) (%)	OA(SVM) (%)	Kappa (SVM) (%)
Backscatter-intensity	66.51	60.93	62.28	55.99	63.05	56.90
Coherence-magnitude	61.63	55.23	59.67	52.94	61.88	55.53
InSAR-phase	42.95	35.03	50.91	42.72	52.62	46.16
Backscatter-intensity & coherence-magnitude	72.43	68.65	69.97	64.97	72.15	68.38
Backscatter-intensity & InSAR-phase	71.84	67.14	70.27	65.32	72.78	68.24
Coherence-magnitude & InSAR-phase	64.12	58.14	61.98	55.64	61.89	55.54
Backscatter-intensity & Coherence-magnitude & InSAR-phase	72.93	68.42	71.56	66.82	72.91	68.39

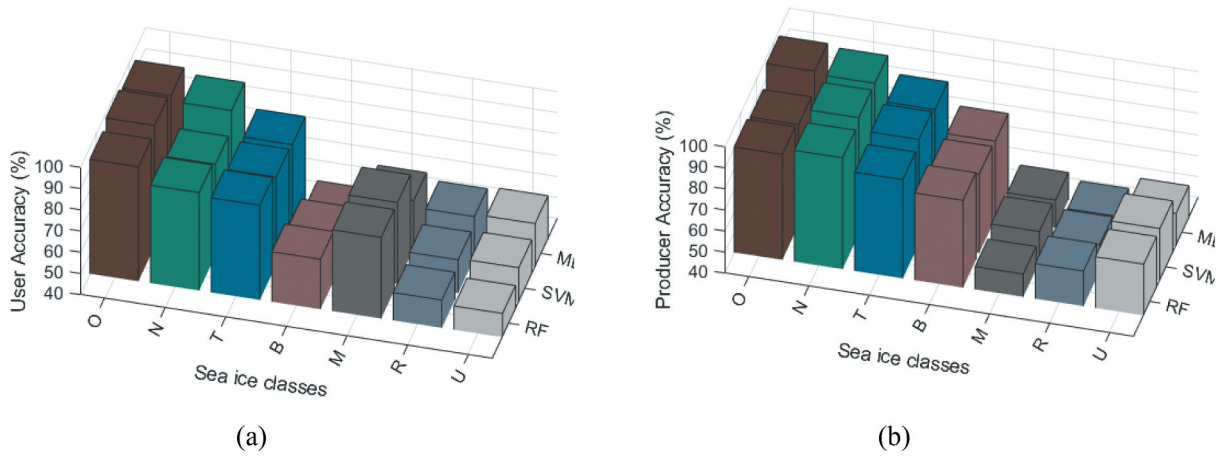


Figure 5. (a) User accuracy and (b) producer accuracy of RF, ML and SVM classified map based on backscatter-intensity & coherence-magnitude & InSAR-phase for water and sea ice classes (U = Undeformed ice, R = Ridged ice, M = Moderately deformed ice, B = Brash ice, T = Thick level ice, N = New ice, O = Open water).

CMs for produced maps in RF-experiments indicated that:

1) Combinations of all three features had the best OA of 72.93% and Kappa coefficient of 0.68.

2) Backscatter-intensity & coherence-magnitude and backscatter-intensity & InSAR-phase combinations were following closely with OAs of 72.43% and 71.84% (Kappa of 0.68 and 0.67), respectively

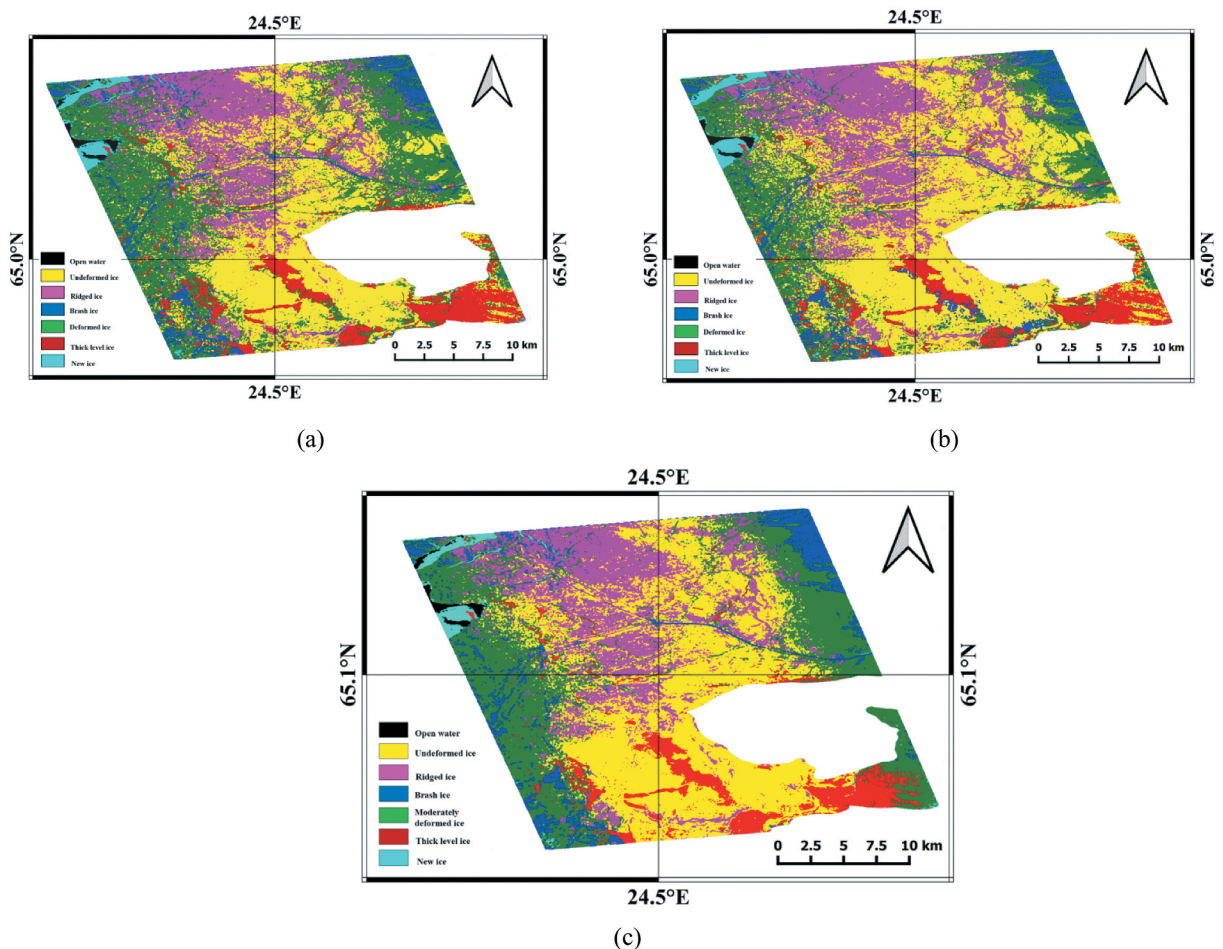


Figure 6. Final classification map using combined backscatter-intensity & coherence-magnitude & InSAR-phase with (a) RF; (b) ML; (c) SVM classifications.

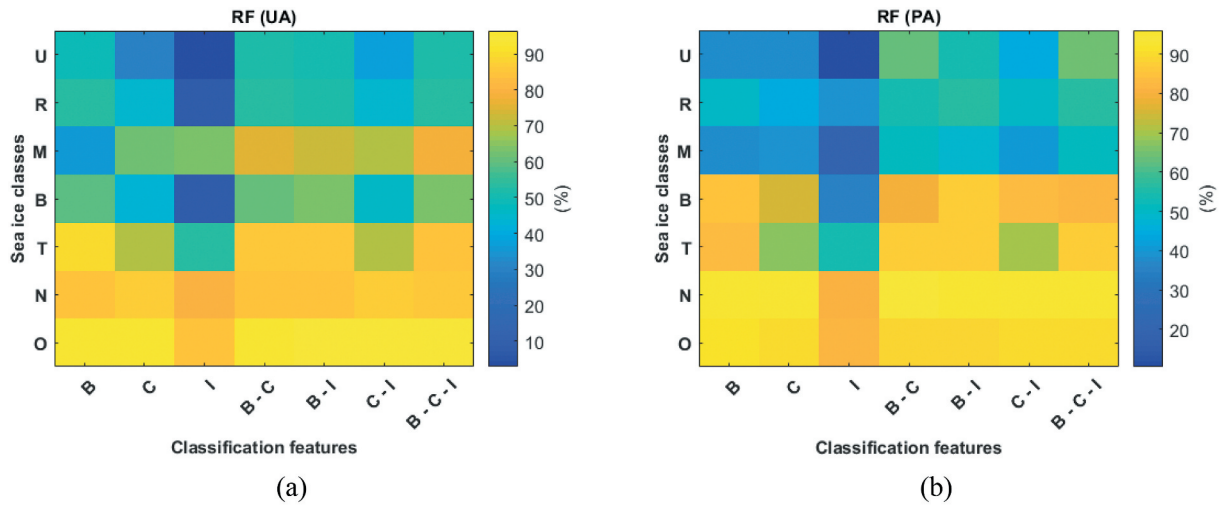


Figure 7. (a) UA and (b) PA in RF classifier for water and sea ice classes (U = Undeformed ice, R = Ridged ice, M = Moderately deformed ice, B = Brash ice, T = Thick level ice, N = New ice, O = Open water), classification features (B = Backscatter-intensity, C = Coherence-magnitude, I = InSAR-phase).

Table 4. The highest and lowest UAs and PAs for input data in RF classifier (B = Backscatter-intensity, C = Coherence-magnitude, I = InSAR-phase).

Classification features	Class or classes with highest/lowest UA in RF (%)	Class or classes with highest/lowest PA in RF(%)
B	Open water (95.49)/Moderately deformed ice (35.09)	New ice (96.08)/Undeformed ice (37.40)
C	Open water (95.55)/Undeformed ice (29.89)	New ice (92.31)/Undeformed ice (37.32)
I	Open water (84.16)/Undeformed ice (2.91)	Open water (82.49)/Undeformed ice (10.40)
B – C	Open water (96.43)/Undeformed ice (51.31)	New ice (94.66)/Moderately deformed ice (50.94)
B – I	Open water (94.11)/Undeformed ice (50.93)	New ice (95.42)/Moderately deformed ice (48.61)
C – I	Open water (94.72)/Undeformed ice (42.91)	New ice (92.32)/Moderately deformed ice (40.53)
B – C – I	Open water (93.87)/Undeformed ice (51.17)	New ice (92.76)/Moderately deformed ice (50.77)

(Table 3). Figure 7(a, b) and Table 4 summarize performance of RF in all experiments for different ice-cover classes. Figure 7(a, b) showed UAs and PAs of single and combination features in RF classifier, respectively, and Table 4 lists the classes which achieved the highest and lowest UAs and PAs for each single feature and their different combinations, respectively. The computation time for RF classification step was almost 5 min per any image feature and it slightly increased when using combinations of two or three features.

CMs in ML-experiments indicated that combinations of all three features had the best OA of 71.56% and Kappa accuracy of 66.82, although backscatter-intensity & InSAR-phase and also backscatter-intensity & coherence-magnitude combinations were following closely with OAs of 70.27% and 69.97% (Kappa accuracies of 65.32 and 64.97), respectively (Table 3). Similar performance was observed in RF classification experiments, though the accuracies were somewhat higher with RF compared to ML.

Figure 8(a, b) and Table 5 summarize performance of ML in all experiments for different ice-cover classes. Figure 8(a, b) shows UAs and PAs of single and combination features in ML classifier, respectively, and Table 5 lists the classes which achieved the highest

and lowest UAs and PAs for each single and combination of input data. The computation time for ML classification was 12 to 15 seconds per any image feature and it slightly increased when using combination of two or three features.

CMs in SVM-experiments also indicated that combinations of all three features had the best OA of 72.91% and Kappa accuracy of 0.68, although backscatter-intensity & InSAR-phase and also backscatter-intensity & coherence-magnitude combinations were following closely with OAs of 72.78% and 72.15% (Kappa accuracies of 0.68 and 0.68), respectively (Table 3). Results was similar with RF and ML classification experiments. The accuracies were somewhat higher with RF classification and a bit lower with ML classification.

Figure 9(a, b) and Table 6 summarize performance of SVM in all experiments for different ice-cover classes. Figure 9(a, b) show UAs and PAs of single and combination features in SVM classifier, respectively, and Table 6 lists the classes which achieved the highest and lowest UAs and PAs for each single and combination of input data. The computation time for SVM classification was about 30 s per any image feature, and it increased when using combination of two or three features.

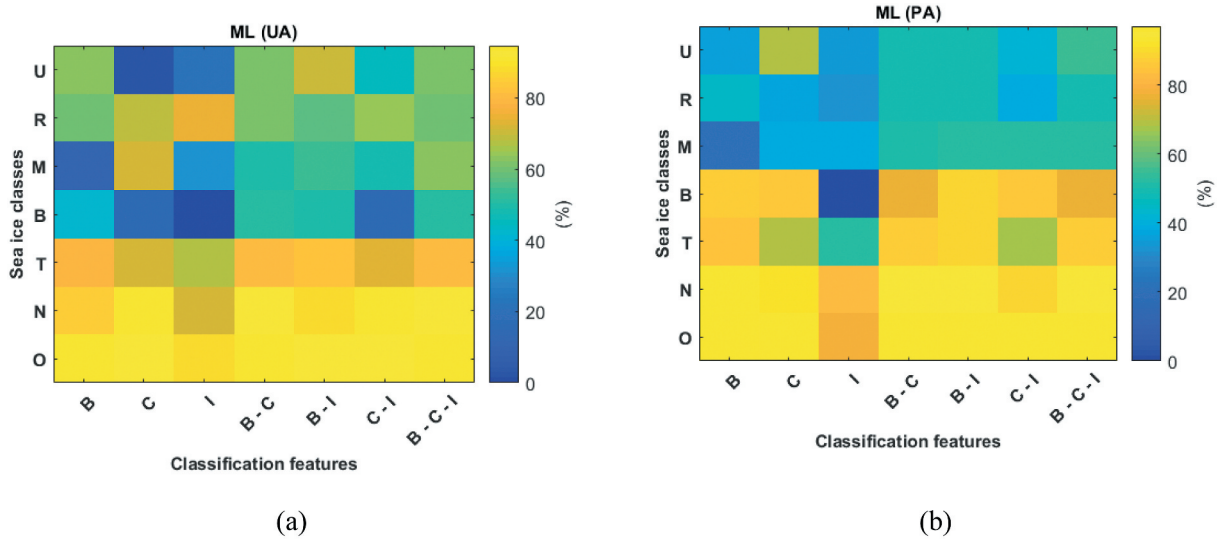


Figure 8. (a) UA and (b) PA in ML classifier for water and sea ice classes (U = Undeformed ice, R = Ridged ice, M = Moderately deformed ice, B = Brash ice, T = Thick level ice, N = New ice, O = Open water), classification features (B = Backscatter-intensity, C = Coherence-magnitude, I = InSAR-phase).

Table 5. The highest and lowest UAs and PAs for input data in ML classifier (B = Backscatter-intensity, C = Coherence-magnitude, I = InSAR-phase).

Classification features	Class or classes with highest/lowest UA in ML (%)	Class or classes with highest/lowest PA in ML (%)
B	Open water (94.61)/Moderately deformed ice (11.46)	Open water (93.09)/Moderately deformed ice (20.37)
C	New ice (93.86)/Undeformed ice (2.61)	Open water (96.02)/Ridged ice (36.90)
I	Open water (88.66)/Brash ice (0)	New ice (83.09)/Brash ice (0)
B – C	Open water (94.64)/Moderately deformed ice (48.81)	Open water (97.07)/Undeformed ice (48.57)
B – I	Open water (92.61)/Brash ice (49.52)	New ice (94.94)/Undeformed ice (49.35)
C – I	New ice (93.95)/Brash ice (15.78)	Open water (95.78)/Ridged ice (38.41)
B – C – I	Open water (94.55)/Brash ice (51.03)	Open water (96.69)/Ridged ice (49.86)

4.2. Comparison of classification approaches

Table 3 shows that RF had higher OAs than ML in all single and combination features except in InSAR-phase feature. RF acted better than ML in all cases including backscatter-intensity (4.23%), coherence-magnitude

(1.96%), backscatter-intensity & coherence-magnitude (2.46%), backscatter-intensity & InSAR-phase (1.57%), coherence-magnitude & InSAR-phase (2.14%), and backscatter-intensity & coherence-magnitude & InSAR-phase (1.37%) combinations. RF and SVM classifiers

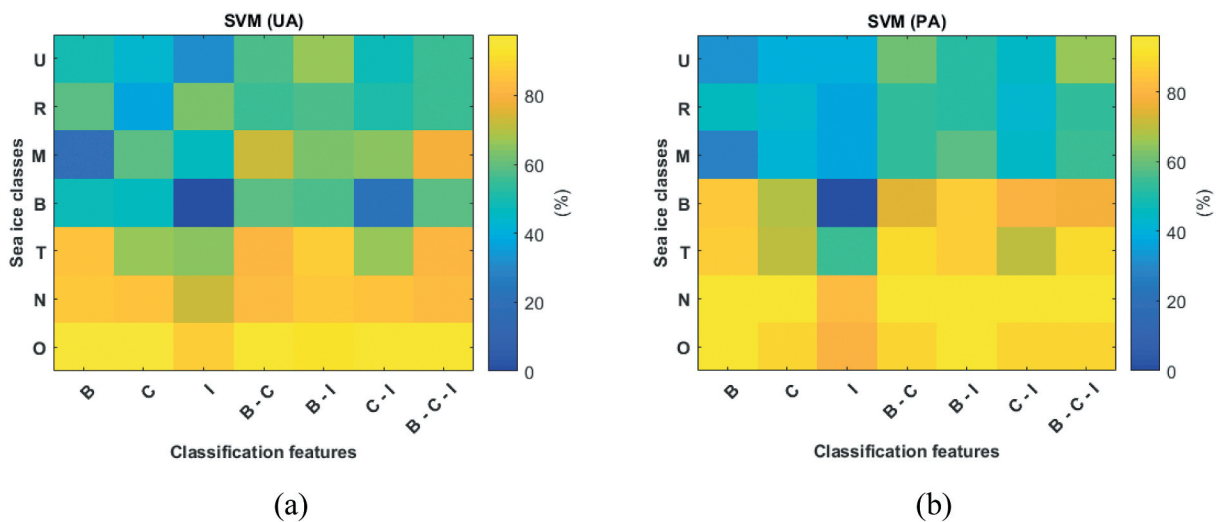


Figure 9. (a) UA and (b) PA in SVM classifier for water and sea ice classes (U = Undeformed ice, R = Ridged ice, M = Moderately deformed ice, B = Brash ice, T = Thick level ice, N = New ice, O = Open water), classification features (B = Backscatter-intensity, C = Coherence-magnitude, I = InSAR-phase).

Table 6. The highest and lowest UAs and PAs for input data in SVM classifier (B = Backscatter-intensity, C = Coherence-magnitude, I = InSAR-phase).

Classification features	Class or classes with highest/lowest UA in SVM (%)	Class or classes with highest/lowest PA in SVM (%)
B	Open water (94.90)/Moderately deformed ice (19.77)	New ice (95.96)/Moderately deformed ice (27.59)
C	Open water (95.88)/Ridged ice (37.39)	New ice (92.82)/Undeformed ice (39.18)
I	Open water (87.84)/Brash ice (0)	New ice (82.68)/Brash ice (0)
B – C	Open water (97.72)/Ridged ice (55.61)	New ice (96.23)/Ridged ice (52.68)
B – I	Open water (92.89)/Ridged ice (56.92)	New ice (95.16)/Ridged ice (52.34)
C – I	Open water (94.45)/Brash ice (22.41)	New ice (91.77)/Ridged ice (42.87)
B – C – I	Open water (96.94)/Ridged ice (55.62)	New ice (95.43)/Ridged ice (52.76)

acted almost in same manner and differences in coherence-magnitude, backscatter-intensity & coherence-magnitude, backscatter-intensity & InSAR-phase and backscatter-intensity & coherence-magnitude & InSAR-phase were near to zero. RF acted better than SVM in cases including backscatter-intensity (3.46%) and coherence-magnitude & InSAR-phase (2.23%) combinations except in InSAR-phase feature that it was 9.67% less than SVM classification.

UA calculations in Figure 7(a), Figure 8(a) and Figure 9(a) show that difference between all classifiers (RF, ML, SVM) for sea ice classes including undeformed ice, ridged ice, moderately deformed ice and brash ice for classification features (single and combination features) was strong. RF had lower UAs for undeformed ice and ridged ice in order of 7–20% and 6–67% compared to ML and 0.7–29% and 2–56% compared to SVM. In comparison to RF and ML, the undeformed ice difference was strongest when backscatter-intensity & InSAR-phase combination was used (19.93%). In addition, ridged ice difference was strongest in InSAR-phase feature (66.62%). RF was more powerful than ML for moderately deformed ice and brash ice in order of 15–33% and 7–30%, respectively. The strongest difference for moderately deformed ice belonged to InSAR-phase feature (32.14%). The brash ice difference was strongest when coherence-magnitude & InSAR-phase combination (29.94%) was used. Although there were one or two exception classes, that ML or RF acted better. For example, coherence-magnitude was the only case that RF acted better than ML in undeformed ice (27.29%) and ML was powerful than RF in moderately deformed ice (9.88%). In comparison, RF and SVM, the undeformed ice (28.46%) and ridged ice (55.18%) had strongest difference when InSAR-phase was used. RF was more powerful than SVM for moderately deformed ice and brash ice in order of 0.02–18% and 2–24%, respectively. The strongest difference for moderately deformed ice belonged to InSAR-phase feature (17.06%). The brash ice difference was strongest when coherence-magnitude & InSAR-phase combination (23.31%) was used. In here also, there were one or two exception classes that SVM or RF acted better. For example, coherence-magnitude was the

only case that RF acted better than SVM in ridged ice (7.53%) and SVM was powerful than RF in brash ice (3.78%).

Difference between RF and ML classifiers for sea ice classes including new ice, thick level ice, and open water was not significant. These differences also were not significant between RF and SVM. In comparison RF and ML, in all single and combination features for new ice; ML had higher UAs than RF with improvements 0.1–9%. The strongest difference was for backscatter-intensity & coherence-magnitude combination (8.70%). InSAR-phase was the only case that had decreasing value from ML to RF with 8.09%. For open water and thick level ice, differences between RF and ML classifiers were in order of 2–14% and 0.6–3%.

In comparison RF and SVM, in all single and combination features for new ice; RF had higher UAs than SVM with improvements 1–7%. The strongest difference was for InSAR-phase (6.82%).

Backscatter-intensity and backscatter-intensity & InSAR-phase were cases that SVM acted better than RF in order of 1.13% and 2.28% for new ice. For open water and thick level ice, differences between RF and SVM classifiers were in order of 0.3–4 and 2–5%.

Figure 7(b), Figure 8(b) and Figure 9(b) show PAs calculations. Here, significant differences between RF with ML and SVM classifiers were found for undeformed ice (1–33%, 0.4–30%), ridged ice (4–12%, 1–8%), moderately deformed ice (0.02–20%, 2–18%) and brash ice (1–35%, 0.09%–35%). Like UAs, difference between RF with ML and SVM classifiers for sea ice classes including new ice (0.1–4%; 0.1–3%), thick level ice (0.4–3%; 0.2–3%) and open water (2–9%; 0.3–5%) was not significant, respectively.

Thus, we can conclude that differences between RF with ML and SVM classifiers were remarkable for undeformed ice, ridged ice, moderately deformed ice and brash ice but were not considerable for new ice, thick level ice and open water classes.

Based on UA calculations for RF (Table 4), the best detected class was open water with UAs in order of 84.16% to 95.55% (in all classification features) whereas undeformed ice was hardest to discriminate in order of 2.29% to 51.17% (in all classification features except in backscatter-intensity feature). Same calculations were done for PAs (Table 4), the best

detected class was new ice with PAs in order of 92.31% to 96.08% (in all classification features except InSAR-phase feature) whereas undeformed ice was hardest classes to discriminate with PAs in order of 10.40% to 37.40% (in single features) and moderately deformed ice was also hard to discriminate with PAs in order of 40.53% to 50.94% (in combination features).

Based on UA calculations for ML (Table 5), the best detected classes were open water with UAs of 88.66% to 94.64% and new ice with UAs in range of 93.86 to 93.95% whereas brash ice was hardest class to discriminate in four classification features with UAs in order of 15.78 to 51.03%. Brash ice in InSAR-phase feature was not discriminated as all. Moderately deformed ice with UAs in order of 11.46 to 48.81% and Undeformed ice with 2.61% were also difficult to discriminate. Same calculations were done for PAs (Table 5), open water with PAs in order of 93.09 to 97.07% (in most classification features) and new ice with PAs in order of 83.09 to 94.94% were the best detected classes. Brash ice was not discriminated at all with one classification feature. Other classes particularly hard to discriminate were ridged ice with PAs in order of 36.90 to 49.86%, undeformed ice with PAs in order of 48.57% to 49.35 and moderately deformed ice with PA of 20.37%.

Based on UA calculations for SVM (Table 6), the best detected class was open water with UAs of 87.84% to 97.72% whereas ridged ice was hardest class to discriminate in four classification features with UAs in order of 37.39 to 56.92%. Brash ice in InSAR-phase feature was not discriminated at all and it was low also in coherence-magnitude & InSAR phase combination (22.41%). Moderately deformed ice with UAs in order of 19.77% was also difficult to discriminate in backscatter-intensity feature. Same calculations were done for PAs (Table 6), new ice with PAs in order of 82.68% to 96.23% was the best detected class. Brash ice was not discriminated at all with one classification feature. Other classes particularly hard to discriminate were ridged ice with PAs in order of 42.87 to 52.76%, undeformed ice with PAs in order of 39.18% and moderately deformed ice with PA of 27.59%.

Considered approaches were partly successful in detecting the brash ice, but the properties of the type of brash ice can be found also in naturally formed ice regimes clearly representing something else than brash ices. Therefore, we suggest other methods for discriminating brash ice from the rest of the ice, e.g., by segmentation and shape feature detection (Berthod et al. 1996).

4.3. Classification improvement by adding InSAR features

Backscatter-intensity feature is regularly used for sea ice classification in most ice services around the world.

In this study, OAs of RF, ML and SVM based on backscatter-intensity feature were in order of 66.51, 62.28, and 63.05%, respectively (Table 3).

Coherence-magnitude feature also had high OAs in three classifiers in order of 61.63, 59.67, and 61.88%. This result proves being valuable previous studies regarding connection between backscatter-intensity and coherence-magnitude features (Dammert, Leppäranta, and Askne 1998; Berg, Dammert, and Eriksson 2015; Laanemäe, Uiboupin, and Rikka 2016).

InSAR-phase feature had OAs in order of 42.95% (RF), 50.91% (ML) and 52.62% (SVM). In our opinion, InSAR-phase feature could not fully reveal its value in contrast to backscatter-intensity and coherence-magnitude features. The reason is using an image with relatively large Height Of Ambiguity (HOA) of 30.84 m in this study. Too large HOAs decrease sensitivity of interferometry to detect sea ice roughness and ridges while in our case, this could aid better discrimination between ice types. The best option to examine in future would be images with smaller HOAs similar to “TanDEM-X Science Phase” mode (Dierking, Lang, and Busche 2017). Detailed discussion about “TanDEM-X Science Phase” mode in this context can be found in Section 4.4.

In this study, adding coherence-magnitude to backscatter-intensity feature improved classification results in 5.92, 7.69, and 9.1% in RF, ML, and SVM classifiers, respectively. This improvement was obvious in backscatter-intensity & InSAR-phase combination representing 5.33%, 7.99% and 9.73% in all experiments (RF, ML, SVM). The strongest improvements were achieved when three features were combined with each other, and represented 6.42% in RF, 9.28% in ML and 9.86% in SVM.

Using InSAR features with backscatter intensity increased classification accuracy for moderately deformed ice (UA: 43.15%, PA: 13.25%) in RF, (UA: 51.27%, PA:32.67%) in ML and (UA: 58.45%, PA: 27.00%) in SVM classifiers. Increased PA accuracies are visible in undeformed ice ($PA_{RF} = 26.9\%$, $PA_{ML} = 19.56\%$, $PA_{SVM} = 32.38\%$), ridged ice ($PARF = 6.58\%$, $PA_{ML} = 5.2\%$, $PA_{SVM} = 7.14\%$) and thick level ice ($PA_{RF} = 3.76\%$, $PA_{ML} = 3.55\%$, $PA_{SVM} = 3.66\%$). As it was expected, adding InSAR features did not add any value to open water and new ice classification results in comparison with only using backscatter intensity. Using three features did not help to better classification of brash ice and as we mentioned in Section 4.1, thus, using other methods for discriminating brash ice from the rest of the ice is strongly suggested. These results emphasize the role of InSAR features (InSAR-phase and coherence magnitude features) in supporting sea ice operational mapping service.

4.4. Effects of image acquisition geometry on ice type classification

Knowledge of the angular dependence of different ice types is necessary to account for automatic sea ice classification of SAR imagery because it is impeded by the incidence angle dependence of backscatter intensities. Several studies at C-band were considering the incidence angle dependence of the sea ice backscattering coefficient (σ°) for different ice types in different polarizations and sea ice conditions (Liu, Guo, and Zhang 2018; Zakhvatkina et al. 2013; Aldenhoff et al. 2020; Mäkynen et al. 2002; Brath, Kern, and Stammer 2013; Gill et al. 2015; Onstott 1992; Mäkynen et al. 2014).

When the swath covers big range of incidence angles like Sentinel-1, the large range of incidence angles cause the backscatter signatures of the same sea ice type to vary across the swath. In this case, two different approaches have been used to determine the incidence angle dependence. One of them is direct slope estimation from backscatter intensity versus incidence angle plots. Another one is, the determination of the σ° versus θ_0 dependence are based on SAR image pairs acquired on ascending and descending orbits over the same sea ice area with a short time difference (Aldenhoff et al. 2020) and then incidence angle normalization is regularly applied for various image classification tasks, e.g., (Lang et al. 2016; Zakhvatkina et al. 2017; Murashkin et al. 2018). In the context of this study, the influence of various incidence angles on backscatter intensity in TanDEM-X mission is not possible to assess, as our analysis is based on one image with relatively narrow swath (42.33–44.46). Acquiring multi-incidence angle dataset is also problematic, as sea ice situation changes rapidly and a dedicated campaign would be needed. Leppäranta, Kuittinen, and Askne (1992) mentioned that backscatter level as well as the ability to distinguish ice types is sensitive to the incidence angle, and thus our results are valid for the incidence angle around the used value. Despite this narrow swath, incidence angle normalization has been done as part of image orthorectification. In future work, effects of varying incidence angle on InSAR based ice classification can be studied using either airborne SAR data, or potentially imagery of small-sat constellations like ICEYE.

Variation of incidence angle is also important in the coherence estimation. Laanemäe, Uiboupin, and Rikka (2016) shows that the best result for ice type discrimination over coherence feature was achieved when SAR images with a high incidence angles were chosen. Laanemäe compared two images with one day apart with similar meteorological conditions in incidence angles 23.4° and 44.9° and showed that the separation of ice and different ice types from low

incidence angle imagery was better in high incidence angle compare with low incidence angle. Based on this, we tried to choose an image with high incidence angle to get the best result for sea ice classification over coherence. Further experiments with larger dataset are needed to assess effects of incidence angle variation over coherence feature for sea ice application.

Regarding the effect of different perpendicular baselines, Dierking, Lang, and Busche (2017) suggested having high sensitivity for object elevation detection. This requires image pair with a large cross-track baseline. In this study, we used a scene with high perpendicular baseline around 240.38 m with short along track baseline. Further studies are possible when collecting several InSAR pairs over the same area within short time interval, and again can be possible with airborne or small-sat SAR campaign only, e.g. with ICEYE satellites (Antropov et al. 2018).

4.5. Comparison with previous studies

To the best of our knowledge, a sea ice classification algorithm based on coherence-magnitude and backscatter-intensity features was used at least once before in the Baltic Sea, over coastal sea ice in the Gulf of Riga (Laanemäe, Uiboupin, and Rikka 2016). Laanemäe, Uiboupin, and Rikka (2016) classified open water and sea ice types based on the threshold values of the backscatter-intensity and coherence-magnitude for fast ice, thin smooth ice, pancake ice and open water. To relate the backscatter-intensity and coherence-magnitude values with the ice types, Regions of Interest (ROIs), based on field observations and optical satellite imagery, were selected to represent the observed different ice types and open water. Their case did not contain any rough ice in contrast to ours. The twin satellites (TanDEM-X and TerraSAR) were operated in the so-called pursuit monostatic mode with an along-track baseline of 20 km, corresponding to 2.6 s time interval (Scheiber et al. 2011). Coherence-magnitude feature was calculated by using two VV and HH pursuit monostatic data and HH-Monostatic data were used for backscattering calculations.

Before proceeding with the discussion, it is good to mention that thin smooth ice term in previous studies (Laanemäe, Uiboupin, and Rikka 2016; Geldsetzer and Yackel 2009) and new ice in our paper essentially mean the same, and they are comparable even if the names differ. Open water and new ice (thin smooth ice in (Laanemäe, Uiboupin, and Rikka 2016) and thin sea ice in (Geldsetzer and Yackel 2009) are common surface types between previous studies (Laanemäe, Uiboupin, and Rikka 2016; Geldsetzer and Yackel 2009) and ours. Geldsetzer and Yackel (2009) indicated that discrimination between open water and new

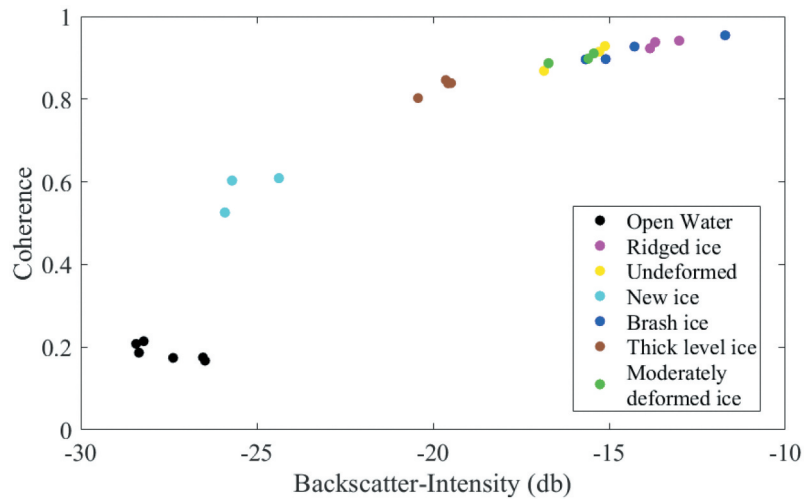


Figure 10. Coherence-magnitude and backscatter-intensity values of water and sea ice types for plots using pair HH-bistatic data for coherence-magnitude calculation and HH-bistatic data for backscatter-intensity calculations.

ice was very difficult due to similarity in backscatter-intensity values. Laanemäe, Uiboupin, and Rikka (2016) tried to solve this difficulty by adding coherence feature to backscatter feature values, but Figure 1 in (Laanemäe, Uiboupin, and Rikka 2016) showed that the same problem remained for the coherence-magnitude values as well. In our study, we examined backscatter-intensity and coherence-magnitude features and indicated that water and new ice are well discriminated by backscatter-intensity and coherence-magnitude features. This success can be explained by the type of TanDEM-X data that were used in this study. Bistatic imaging mode would be better option compared to monostatic imaging mode (Laanemäe, Uiboupin, and Rikka 2016) in open water and new ice discrimination. In bistatic acquisition, wind speed would not cause temporal decorrelation of interferometric coherence.

Open water/ice separation is one of the key question in sea ice remote sensing. In our study, this good separation is not only between open water and new ice. It was also apparent between open water and other types of ice in Figure 10 by using backscatter-intensity and coherence-magnitude features. Although we need to do same work over more cases of study to evaluate the consistency of the classification.

InSAR-phase feature was used recently in a paper by Dierking, Lang, and Busche (2017) for retrieving the ice surface topography. Dierking used InSAR-phase data acquired during “TanDEM-X Science Phase”. Both “Standard operation” and “TanDEM-X Science Phase” modes were used to map topography and build digital elevation models. “TanDEM-X Science Phase” was more accurate than “Standard operation” due to bigger cross track baseline and smaller HOAs. So, it would be concluded that using “TanDEM-X Science Phase” mode is better and more

accurate option to detect sea ice topography than “Standard operation” mode.

In this study, analysis was done using scene acquired in “Standard operation” mode. Standard operation mode has been designed for topographic mapping of the Earth’s land masses. Its achievable relative accuracies are 2–4 m vertically and 3 m horizontally at a horizontal sampling of 12 m. However, using InSAR features even in this setup was useful for discriminating sea ice classes, though not to its full possible potential.

5. Conclusions and future research

In this study, different features of TanDEM-X imagery were used for assessment of sea ice classes (undeformed ice, ridged ice, moderately deformed ice, brash ice, thick level ice, new ice) and open water over the Baltic Sea. Three types of supervised classifiers, RF, ML, and SVM algorithms were applied over single features and their different combinations. The best results were provided by combined backscatter-intensity & coherence-magnitude & InSAR-phase with OAs 72.93%, 71.56% and 72.91% in RF, ML, and SVM classifiers. Combined features outperformed single features in all sea ice classification scenarios. The RF algorithm seems to be more suitable approach than SVM and ML due to higher OAs, however, at the expense of somewhat longer processing time (5 min for RF versus 15 seconds for ML and 30 s SVM at Intel i5-7200 U machine).

This study also proved advantage of interferometric features (coherence-magnitude & InSAR-phase) in combination with backscatter-intensity feature over single backscatter-intensity feature by showing improvements OAs in order of 6.42% in RF, 9.28% in ML and 9.86% in SVM classifiers. For most of

separated classes, the improvement was even stronger; and the strongest one was moderately deformed ice with improvements in order of (UA: 43.15%, PA: 13.25%) in RF, (UA: 51.27%, PA: 32.67%) in ML and (UA: 58.45%, PA: 27.00%) in SVM classifiers. Brash ice was not well discriminated by our method, so using other methods for discriminating brash ice from the rest of the ice is suggested. Also differences between RF with ML and SVM classifiers were remarkable for undeformed ice, ridged ice, moderately deformed ice and brash ice but were not considerable for new ice, thick level ice and open water classes.

This study is the first approach to thoroughly evaluate backscatter-intensity, coherence-magnitude and InSAR-phase features at X-band and their different combinations in sea ice classification. Previously, water and new ice were particularly hard to discriminate due to their similar backscattering values (Laanemäe, Uiboupin, and Rikka 2016; Geldsetzer and Yackel 2009). Even adding coherence-magnitude (Laanemäe, Uiboupin, and Rikka 2016) did not improve the discrimination between these classes, but this issue was successfully solved in our study. As our image was acquired in bistatic InSAR imaging mode, no temporal decorrelation affected InSAR coherence. Bistatic TanDEM-X data were particularly useful for discriminating open water and new ice. Our future efforts might focus on using various advanced texture feature extraction techniques from intensity, coherence and phase features to be tested with suitable classifiers.

Acknowledgments

The authors would like to thank ESA for SNAP software. We also thank Mr. Andreas Braun who offered invaluable guidance on the application of the SNAP and Markku Kulmala at Institute for Atmospheric and Earth System Research (INAR), University of Helsinki for valuable support. We thank two anonymous reviewers for recommendations, which helped improve the final manuscript.

Funding

This research was supported by Academy of Finland under Grant no.296628.

Notes on contributors

Marjan Marbouti is a PhD student in geophysics at Institute for Atmospheric and Earth System Research (INAR), Helsinki University. She received her bachelor's degree in physics from Islamic Azad university-Dezfool branch, Dezfool, Iran in 2009 and his master degree in physics-astronomy from Islamic azad university-Central Tehran branch, Tehran, Iran, in 2011. His research interests is remote sensing of sea ice, ocean color properties, and atmospheric properties.

Oleg Antropov is a Senior Scientist at VTT Technical Research Center of Finland. He received the M.S. degree in computer science and the Candidate of Sciences degree in radio physics from Dnepropetrovsk National University, Ukraine, in 2006 and 2010, respectively, and PhD degree in space technology from Aalto University, Espoo, Finland, in 2014. His research interests include application of multi-parametric SAR data for various environmental applications.

Jaan Praks is an Assistant Professor (tenure track) at Aalto University and leader of Aalto Space Technology and Microwave Remote Sensing research group. He received an MSc. in physics from University of Tartu and PhD. in space technology from Aalto University 2012. His research interests include microwave remote sensing, especially SAR Interferometry and SAR polarimetry, and nanosatellite technology. During his career, he has participated in numerous remote sensing projects and measurement campaigns, instrument developments and led the development of Aalto-1, Aalto-2, Aalto-3, and Foresail nanosatellites. Currently, he is leading Satellite Platforms team in Finnish Centre of Excellence in Research of Sustainable Space. From his research projects have started many New Space and Earth Observation start-up companies in Finland.

Patrick B. Eriksson is an ice expert and product manager at the Oceanographic Services of the Finnish Meteorological Institute in Helsinki. He has a M.Sc. degree in polar oceanography from University of Helsinki. He is an ice analyst at the Finnish Ice Service with solid routine in ice monitoring, ice observation, and remote sensing and broad customer relations to winter navigation operations.

Vahid Arabzadeh is a Ph.D. student at Aalto University, school of science. He received two MSc. in Mechanical engineering and system control. His main research interest is energy system modeling, optimization, AI, and data analysis.

Eero Rinne is the head of polar oceanography and sea ice research group at the Finnish Meteorological Institute. He received an MSc. in satellite technology from Helsinki University of Technology in 2005 and a PhD in geophysics from University of Edinburgh in 2011. His main research interest is novel satellite remote sensing methods for the cryosphere.

Matti Leppäranta is an emeritus professor of geophysics in the University of Helsinki, Finland. He received his MSc degree in mathematics in 1976 and PhD in physical oceanography in 1981 from the University of Helsinki. His research interests include the physics of freezing seas and lakes, and has published the books, *Drift of sea ice* (two editions) and *Freezing lakes and the evolution of their ice cover*.

ORCID

Marjan Marbouti  <http://orcid.org/0000-0002-8892-2290>
 Oleg Antropov  <http://orcid.org/0000-0001-8576-404X>
 Matti Leppäranta  <http://orcid.org/0000-0002-4754-5564>

Data availability statement

TanDEM-X data that support the findings of this study are available from DLR. Restrictions apply to the availability of these data, which were used under license for this study (<https://tandemx-science.dlr.de/pdfs/TSX-TDX-user-license->

v2.2.pdf). The manual image classification analysis done by an ice analyst was generated at the Ice Service of the Finnish Meteorological Institute. Derived data supporting the findings of this study are available from the corresponding author PBE on request.

References

- Ahmad, A., and S. Quegan. 2012. "Analysis of Maximum Likelihood Classification on Multispectral Data." *Applied Mathematical Sciences* 6 (129): 6425–6436. doi:10.12988/ams.2013.34214.
- Aldenhoff, W., L. E. B. Eriksson, Y. Ye, and C. Heuzé. 2020. "First-Year and Multiyear Sea Ice Incidence Angle Normalization of Dual-Polarized Sentinel-1 SAR Images in the Beaufort Sea." *IEEE Journal of Selected Topics in Applied Earth Observations and Remote Sensing* 13: 1540–1550. doi:10.1109/JSTARS.2020.2977506.
- Anthony, G., H. Greg, and M. Tshilidzi. 2007. "Classification of Images Using Support Vector Machines." arXiv:0709.3967.
- Antropov, O., J. Praks, M. Kauppinen, P. Laurila, V. Ignatenko, and R. Modrzewski. 2018. "Assessment of Operational Microsatellite Based SAR for Earth Observation Applications." In *Proceedings of second URSI Atlantic Radio Science Meeting (AT-RASC)*, Meloneras, May-1 June 28 May-1. doi: 10.23919/URSI-AT-RASC.2018.8471324.
- Antropov, O., Y. Rauste, H. Astola, J. Praks, T. Häme, and M. Hallikainen. 2014. "Land Cover and Soil Type Mapping from Spaceborne PolSAR Data at L-Band with Probabilistic Neural Network." *IEEE Transactions on Geoscience and Remote Sensing* 52 (9): 5226–5270. doi:10.1109/TGRS.2013.2287712.
- Askne, J., M. Leppäranta, and T. Thompson. 1992. "Bothnian Experiment in Preparation for ERS-1, 1988 (BEPERS-88) – An Overview." *International Journal of Remote Sensing* 13 (13): 2377–2398. doi:10.1080/01431169208904277.
- Barber, D. G., and E. F. LeDrew. 1991. "SAR Sea Ice Discrimination Using Texture Statistics: A Multivariate Approach." *Photogrammetric Engineering and Remote Sensing* 57 (4): 385–395.
- Berg, A., P. B. G. Dammert, and L. E. Eriksson. 2015. "X-Band Interferometric SAR Observations of Baltic Fast Ice." *IEEE Transactions on Geoscience and Remote Sensing* 53 (3): 1248–1256. doi:10.1109/TGRS.2014.2336752.
- Berthod, M., Z. Kato, Y. Shan, and J. Zerubia. 1996. "Bayesian Image Classification Using Markov Random Fields." *Image and Vision Computing* 14 (4): 285–295. doi:10.1016/0262-8856(95)01072-6.
- Bogdanov, A. V., S. Sandven, O. M. Johannessen, V. Y. Alexandrov, and L. P. Bobylev. 2005. "Multisensor Approach to Automated Classification of Sea Ice Image Data." *IEEE Transactions on Geoscience and Remote Sensing* 43 (7): 1648–1664. doi:10.1109/TGRS.2005.846882.
- Brath, M., S. Kern, and D. Stammer. 2013. "Sea Ice Classification during freeze-Up Conditions with Multifrequency Scatterometer Data." *IEEE Transactions on Geoscience and Remote Sensing* 51 (6): 3336–3353. doi:10.1109/TGRS.2012.2222031.
- Breiman, L. 2001. "Random Forests." *Machine Learning* 45 (1): 5–32. doi:10.1023/A:1010933404324.
- Breivik, L.-A., S. Eastwood, and T. Lavergne. 2012. "Use of C-band Scatterometer for Sea Ice Edge Identification." *IEEE Transactions on Geoscience and Remote Sensing* 50 (7): 2669–2677. doi:10.1109/TGRS.2012.2188898.
- Clausi, D. A. 2001. "Comparison and Fusion of Co-occurrence, Gabor, and MRF Texture Features for Classification of SAR Sea Ice Imagery." *Atmosphere-Ocean* 39 (3): 183–194. doi:10.1080/07055900.2001.9649675.
- Clausi, D. A., and B. Yue. 2004. "Comparing Cooccurrence Probabilities and Markov Random Fields for Texture Analysis of SAR Sea Ice Imagery." *IEEE Transactions on Geoscience and Remote Sensing* 42 (1): 215–228. doi:10.1109/TGRS.2003.817218.
- Clausi, D. A., and Y. Zhao. 2002. "Rapid Extraction of Image Texture by Co-occurrence Using a Hybrid Data Structure." *Computers & Geosciences* 28 (6): 763–774. doi:10.1016/S00983004(01)00108-X.
- Clausi, D. A., and Y. Zhao. 2003. "Grey Level Co-occurrence Integrated Algorithm (GLCIA): A Superior Computational Method to Rapidly Determine Co-occurrence Probability Texture Features." *Computers & Geosciences* 29 (7): 837–850. doi:10.1016/S00983004(03)00089-X.
- Dammert, P. B. G., M. Leppäranta, and J. Askne. 1998. "SAR Interferometry over Baltic Sea Ice." *International Journal of Remote Sensing* 19 (16): 3019–3037. doi:10.1080/014311698214163.
- Dierking, W. 2010. "Mapping of Different Sea Ice Regimes Using Images from Sentinel-1 and ALOS Synthetic Aperture Radar." *IEEE Transactions on Geoscience and Remote Sensing* 48 (3): 1045–1058. doi:10.1109/TGRS.2009.2031806.
- Dierking, W. 2013. "Sea Ice Monitoring by Synthetic Aperture Radar." *Oceanography* 26 (2): 100–111. doi:10.5670/oceanog.2013.33.
- Dierking, W., O. Lang, and T. Busche. 2017. "Sea Ice Local Surface Topography from Single-pass Satellite InSAR Measurements: A Feasibility Study." *The Cryosphere* 11: 1967–1985. doi:10.5194/tc-11-1967-2017.
- Dierking, W., and L. T. Pedersen. 2012. "Monitoring Sea Ice Using ENVISAT ASAR-A New Era Starting 10 Years Ago." In *Proceedings of Geoscience and Remote Sensing Symposium (IGARSS)*, IEEE International, Munich, Germany, 22-27 July 2012. doi:10.1109/IGARSS.2012.6351147.
- Dierking, W., and C. Wesche. 2014. "C-Band Radar polarimetry–Useful for Detection of Icebergs in Sea Ice?" *IEEE Transactions on Geoscience and Remote Sensing* 52 (1): 25–37. doi:10.1109/TGRS.2012.2234756.
- Du, P., A. Samat, B. Waske, S. Liu, and Z. Li. 2015. "Random Forest and Rotation Forest for Fully Polarized SAR Image Classification Using Polarimetric and Spatial Features." *ISPRS Journal of Photogrammetry and Remote Sensing* 105: 38–53. doi:10.1016/j.isprsjprs.2015.03.002.
- Fors, A. S. 2016. "Investigations of Summer Sea Ice with X and C-band Multi-polarimetric Synthetic Aperture Radar (SAR)." PhD diss., Arctic University of Norway, Norway.
- Friedrichs, F., and C. Igel. 2005. "Evolutionary Tuning of Multiple SVM Parameters." *Neurocomputing* 64: 107–117. doi:10.1016/j.neucom.2004.11.022.
- Gegiuc, A., M. Similä, J. Karvonen, M. Lensu, M. Mäkynen, and J. Vainio. 2017. "Estimation of Degree of Sea Ice Ridging Based on Dual-Polarized C-band SAR Data." *The Cryosphere* 12 (1): 343–364. doi:10.5194/tc-12-343-2018.

- Geldsetzer, T., and J. Yackel. 2009. "Sea Ice Type and Open Water Discrimination Using Dual Co-polarized C-band SAR." *Canadian Journal of Remote Sensing* 35 (1): 73–84. doi:10.5589/m08-075.
- Gill, J. P. S., J. J. Yackel, T. Geldsetzer, and M. Christopher Fuller. 2015. "Sensitivity of C-band Synthetic Aperture Radar Polarimetric Parameters to Snow Thickness over Landfast Smooth first Year Sea Ice." *Remote Sensing of Environment* 166: 34–49. doi:10.1016/j.rse.2015.06.005.
- Goldstein, R. V., N. M. Osipenko, and M. Leppäranta. 2009. "Relaxation Scales and the Structure of Fractures in the Dynamics of Sea Ice." *Cold Regions Science and Technology* 58 (1–2): 29–35. doi:10.1016/j.coldregions.2009.03.003.
- Hamidi, D., S. Lehner, T. König, and A. Pleskachevsky. 2011. "On the Sea Ice Motion Estimation with Synthetic Aperture Radar." In *Proceedings of the 4th TerraSAR-X Meeting 2011*, Oberpfaffenhofen, Germany, 14–16 February 2011; Volume Vortrags-Nr. CAL0166, pp. 1–10. Item URL in elib: <https://elib.dlr.de/72252/>.
- Han, Y., J. Ren, Z. Hong, Y. Zhang, L. Zhang, W. Meng, and Q. Gu. 2015. "Active Learning Algorithms for the Classification of Hyperspectral Sea Ice Images." *Mathematical Problems in Engineering* 2015. Article ID 124601. doi:10.1155/2015/124601. 2015:1–10.
- Huang, C., L. S. Davis, and J. R. G. Townshend. 2002. "An Assessment of Support Vector Machines for Land Cover Classification." *International Journal of Remote Sensing* 23 (4): 725–749. doi:10.1080/01431160110040323.
- Hurtado, D. M. 2012. "Interferometric Processing of TanDEM-X Images for Forest Height Estimation." Master diss., University of Aalto, Helsinki, Finland.
- Joachims, T. 1998. "Text Categorization with Support Vector Machines—Learning with Many Relevant Features." In *Proceedings of the 10th European Conference on Machine Learning*, Chemnitz, Germany. 137–142. doi: 10.17877/DE290R-5097.
- Karvonen, J. 2004. "Baltic Sea Ice SAR Segmentation and Classification Using Modified Pulse Coupled Neural Networks." *IEEE Transactions on Geoscience and Remote Sensing* 42 (7): 1566–1574. doi:10.1109/TGRS.2004.828179.
- Karvonen, J. 2012. "Operational SAR-based Sea Ice Drift Monitoring over the Baltic Sea." *Ocean Science* 8: 473–483. doi:10.5194/os-8-473-2012.
- Kwok, R., G. Spreen, and S. Pang. 2013. "Arctic Sea Ice Circulation and Drift Speed: Decadal Trends and Ocean Currents." *Journal of Geophysical Research Atmospheres* 118 (5): 2408–2425. doi:10.1002/jgrc.20191.
- Laanemäe, K. 2017. "Estimation of Sea Ice Extent from Sentinel-1 Radar Data in Estonian Coastal Sea." Master diss., Tallinn University of Technology, Marine System Institute at TUT, Tallinn, Estonia.
- Laanemäe, K., R. Uiboupin, and S. Rikka. 2016. "Sea Ice Type Classification in the Baltic Sea from TanDEM-X Imagery." In *Proceedings of EUSAR 2016: 11th European Conference on Synthetic Aperture Radar*, Hamburg, Germany, 6–9 June 2016. Print ISBN: 978-3-8007-4228-8.
- Lang, W., P. Zhang, J. Wu, Y. Shen, and X. Yang. 2016. "Incidence Angle Correction of SAR Sea Ice Data Based on Locally Linear Mapping." *IEEE Transactions on Geoscience and Remote Sensing* 54 (6): 3188–3199. doi:10.1109/TGRS.2015.2513159.
- Leppäranta, M., and R. Hakala. 1992. "The Structure and Strength of First-year Ice Ridges in the Baltic Sea." *Cold Regions Science and Technology* 20 (3): 295–311. doi:10.1016/0165232X(92)90036-T.
- Leppäranta, M., R. Kuittinen, and J. Askne. 1992. "BEPERS Pilot Study: An Experiment with X-band Synthetic Aperture Radar in the Baltic Sea." *Journal of Glaciology* 38 (128): 23–35. doi:10.3189/S0022143000009564.
- Leppäranta, M., and K. Myrberg. 2009. *Physical Oceanography of the Baltic Sea*. Heidelberg, Germany: Springer-Verlag Berlin Heidelberg.
- Leppäranta, M., Y. Sun, and J. Haapala. 1998. "Comparisons of Sea-Ice Velocity Fields from ERS-1 SAR and a Dynamic Model." *Journal of Glaciology* 44 (147): 248–262. doi:10.3189/S0022143000002598.
- Liu, A. K., B. Holt, and P. W. Vachon. 1991. "Wave Propagation in the Marginal Ice Zone: Model Predictions and Comparisons with Buoy and Synthetic Aperture Radar Data." *Journal of Geophysical Research* 96 (C3): 4605–4621. doi:10.1029/90JC02267.
- Liu, H., H. Guo, and L. Zhang. 2018. "SVM-Based Sea Ice Classification Using Textural Features and Concentration from RADARSAT-2 Dual-Pol ScanSAR Data." *IEEE Journal of Selected Topics in Applied Earth Observations and Remote Sensing* 8 (4): 1601–1613. doi:10.1109/JSTARS.2014.2365215.
- Liu, H., X. M. Li, and H. Guo. 2017. "The Dynamic Processes of Sea Ice on the East Coast of Antarctica—A Case Study Based on Spaceborne Synthetic Aperture Radar Data from TerraSAR-X." *IEEE Journal of Selected Topics in Applied Earth Observations and Remote Sensing* 9 (3): 1187–1198. doi:10.1109/JSTARS.2015.2497355.
- Mäkynen, M., and M. Hallikainen. 2004. "Investigation of C- and X-band Backscattering Signatures of Baltic Sea Ice." *International Journal of Remote Sensing* 25 (11): 2061–2086. doi:10.1080/01431160310001647697.
- Mäkynen, M., S. Kern, A. Rösel, and L. T. Pedersen. 2014. "On the Estimation of Melt Pond Fraction on the Arctic Sea Ice with ENVISAT WSM Images." *IEEE Transactions on Geoscience and Remote Sensing* 52 (11): 7366–7379. doi:10.1109/TGRS.2014.2311476.
- Mäkynen, M., T. Manninen, M. Similä, J. Karvonen, and M. Hallikainen. 2002. "Incidence Angle Dependence of the Statistical Properties of C-band HH-polarization Backscattering Signatures of the Baltic Sea Ice." *IEEE Transactions on Geoscience and Remote Sensing* 40 (12): 2593–2605. doi:10.1109/TGRS.2002.806991.
- Marbouti, M., O. Antropov, P. B. Eriksson, J. Praks, V. Arabzadeh, E. Rinne, and M. Leppäranta. 2018. "Automated SEA ICE Classification over the Baltic SEA Using Multiparametric Features of Tandem-X InSAR Images." In *Proceedings of IGARSS 2018-2018 IEEE International Geoscience and Remote Sensing Symposium*, 22–27 July 2018, Valencia, Spain. doi:10.1109/IGARSS.2018.8518996.
- Marbouti, M., J. Praks, O. Antropov, E. Rinne, and M. Leppäranta. 2017. "A Study of Landfast Ice with Sentinel-1 Repeat-pass Interferometry over the Baltic Sea." *Remote Sensing* 9 (8): 833. doi:10.3390/rs9080833.
- Marbouti, M., L. E. B. Eriksson, D. O. Dammann, D. Demchev, J. Jones, A. Berg, and O. Antropov. 2020. "Evaluating Landfast Sea Ice Ridging near Utqiagvik Alaska Using TanDEM-X Interferometry." *Remote Sensing* 12 (8): 1247. doi:10.3390/rs12081247.
- Maslanik, J. A., C. Fowler, J. Stroeve, S. Drobot, J. Zwally, D. Yi, W. Emery. 2007. "A Younger, Thinner Arctic Ice Cover: Increased Potential for Rapid, Extensive Sea-ice Loss." *Geophysical Research Letters* 34 (24): L24501. doi:10.1029/2007GL032043.

- Maurer, E., R. Kahle, F. Mrowka, G. Morfill, A. Ohndorf, and S. Zimmermann. 2016. "Operational Aspects of the TanDEM-X Science Phase," *In Proceedings of 14th International Conference on Space Operations*, Daejeon, Korea, 16–20 May 2016. AIAA 2016–2459. doi: [10.2514/6.2016-2459](https://doi.org/10.2514/6.2016-2459).
- Melgani, F., and L. Bruzzone. 2004. "Classification of Hyperspectral Remote Sensing Images with Support Vector Machines." *IEEE Transactions on Geoscience and Remote Sensing* 42 (8): 1778–1790. doi:[10.1109/TGRS.2004.831865](https://doi.org/10.1109/TGRS.2004.831865).
- Murashkin, D., G. Spreen, M. Huntemann, and W. Dierking. 2018. "Method for Detection of Leads from Sentinel-1 SAR Images." *Annals of Glaciology* 59 (76pt2): 124–136. doi:[10.1017/aog.2018.6](https://doi.org/10.1017/aog.2018.6).
- Ochilov, S., and D. A. Clausi. 2012. "Operational SAR Sea-ice Image Classification." *IEEE Transactions on Geoscience and Remote Sensing* 50 (11): 4397–4408. doi:[10.1109/TGRS.2012.2192278](https://doi.org/10.1109/TGRS.2012.2192278).
- Onstott, R. G. 1992. "SAR and Scatterometer Signatures of Sea Ice. Microwave Remote Sensing of Sea Ice." In *Geophys. Monogr. Ser.*, edited by F. D. Carsey, 73–104. Vol. 68. Washington, D. C.: AGU.
- Oshiro, T. M., P. S. Perez, and J. A. Baranauskas. 2012. "How Many Trees in a Random Forest?" *In Proceedings of 8th International Conference on Machine Learning and Data Mining in Pattern Recognition, MLDM 2012*, Lecture Notes in Computer Science, Volume: 7376, Berlin, Germany, July 13–20. doi: [10.1007/978-3-642-31537-4_13](https://doi.org/10.1007/978-3-642-31537-4_13)
- Palosuo, E., M. Leppäranta, and A. Seinä. 1982. *Formation, Thickness and Stability of Fast Ice along the Finnish Coast*. Vol. 36 vols. Res. Rep. Helsinki, Finland: Winter Navig. Res. Board.
- Park, J.-W., H.-C. Kim, S.-H. Hong, S.-H. Kang, H. C. Graber, B. Hwang and C. M. Lee. 2016. "Radar Backscattering Changes in Arctic Sea Ice from Late Summer to Early Autumn Observed by Space-borne X-band HH-polarization SAR." *Remote Sensing Letters* 7 (6): 551–560. doi:[10.1080/2150704X.2016.1165881](https://doi.org/10.1080/2150704X.2016.1165881).
- Plank, S. 2014. "Rapid Damage Assessment by Means of Multi-Temporal SAR — A Comprehensive Review and Outlook to Sentinel-1." *Remote Sensing* 6 (6): 4870–4906. doi:[10.3390/rs6064870](https://doi.org/10.3390/rs6064870).
- Ressel, R., A. Frost, and S. Lehner. 2015. "A Neural Network-Based Classification for Sea Ice Types on X-Band SAR Images." *IEEE Journal of Selected Topics in Applied Earth Observations and Remote Sensing* 8 (7): 3672–3680. doi:[10.1109/JSTARS.2015.2436993](https://doi.org/10.1109/JSTARS.2015.2436993).
- Ressel, R., and S. Singha. 2016. "Comparing near Coincident Space Borne C and X Band Fully Polarimetric SAR Data for Arctic Sea Ice Classification." *Remote Sensing* 8 (3): 198. doi:[10.3390/rs8030198](https://doi.org/10.3390/rs8030198).
- Ressel, R., S. Singha, S. Lehner, A. Rösel, and G. Spreen. 2016. "Investigation into Different Polarimetric Features for Sea Ice Classification Using X-Band Synthetic Aperture Radar." *IEEE Journal of Selected Topics in Applied Earth Observations and Remote Sensing* 9 (7): 3131–3143. doi:[10.1109/JSTARS.2016.2539501](https://doi.org/10.1109/JSTARS.2016.2539501).
- Rigor, I., and J. M. Wallace. 2004. "Variations in the Age of Arctic Sea-ice and Summer Sea Ice Extent." *Geophysical Research Letters* 31 (9): L09401. doi:[10.1029/2004GL019492](https://doi.org/10.1029/2004GL019492).
- Sadeghi, Y., B. St-Onge, B. Leblon, M. Simard, and K. Papathanassiou. 2014. "Mapping Forest Canopy Height Using TanDEM-X DSM and Airborne LiDAR DTM," *In Proceedings of 2014 IEEE Geoscience and Remote Sensing Symposium*, Quebec City, QC, Canada 13-18 July. doi: [10.1109/IGARSS.2014.6946359](https://doi.org/10.1109/IGARSS.2014.6946359).
- Sandven, S., V. Alexandrov, N. Zakhvatkina, and M. Babiker. 2012. "Sea Ice Classification Using Radarsat-2 Dual-polarisation Data." *In Proceedings of the 4rd International Workshop on Advances in SAR Oceanography*, Tromsø, Norway, 18-22 June 2012.
- Sandven, S., and O. M. Johannessen. 1989. "Ice Edge Motion during MIZEX'87." *In Proceedings of 12th Canadian Symposium on Remote Sensing Geoscience and Remote Sensing Symposium*, Vancouver, Canada, Canada, 10-14 July, doi: [10.1109/IGARSS.1989.576204](https://doi.org/10.1109/IGARSS.1989.576204).
- Scheiber, R., F. De Zan, P. Prats-Iraola, L. Sant'Anna Araújo, M. Künemund, and L. Marotti. 2011. "Interferometric Sea Ice Mapping with TanDEM-X: First Experiments." *In Proceedings of Geoscience and Remote Sensing Symposium (IGARSS), 2011 IEEE International*, Vancouver, BC, Canada, 24-29 July. doi: [10.1109/IGARSS.2011.6050001](https://doi.org/10.1109/IGARSS.2011.6050001).
- Scheuchl, B., D. Flett, R. Caves, and I. Cumming. 2004. "Potential of RADARSAT-2 Data for Operational Sea Ice Monitoring." *Canadian Journal of Remote Sensing* 30 (3): 448–461. doi:[10.5589/m04-011](https://doi.org/10.5589/m04-011).
- Scheuchl, B., I. Hajnsek, and I. Cumming. 2003. "Classification Strategies for Polarimetric SAR Sea Ice Data." *In Proceedings of the Workshop on POLinSAR - Applications of SAR Polarimetry and Polarimetric Interferometry (ESA SP-529)*, Frascati, Italy, January 14–16.
- Scheuchl, B., R. Caves, I. G. Cumming, and G. Staples. 2001. "Automated Sea Ice Classification Using Spaceborne Polarimetric SAR Data." *In Proceedings of Geoscience and Remote Sensing Symposium, IGARSS '01. IEEE 2001 International*, Sydney, NSW, Australia, 9-13 July 2001. doi: [10.1109/IGARSS.2001.978275](https://doi.org/10.1109/IGARSS.2001.978275).
- Seinä, A., and E. Palosuo. 1996. "The Classification of the Maximum Annual Extent of Ice Cover in the Baltic Sea 1720-1995," Meri Report No. 27, Finnish Institute of Marine Research, Finland. 79–91.
- Seinä, A., and J. Peltola. 1991. *Duration of Ice Season and Statistics of Fast Ice Thickness along the Finnish Coast 1961-1990*. Helsinki: Merentutkimuslaitos.
- Shokr, M. 2009. "Compilation of a Radar Backscatter Database of Sea Ice Types and Open Water Using Operational Analysis of Heterogeneous Ice Regimes." *Canadian Journal of Remote Sensing* 35 (4): 369–384. doi:[10.5589/m09-026](https://doi.org/10.5589/m09-026).
- Similä, M., E. Arjas, M. Mäkynen, and M. Hallikainen. 2001. "A Bayesian Classification Model for Sea Ice Roughness from Scatterometer Data." *IEEE Transactions on Geoscience and Remote Sensing* 39 (7): 1586–1595. doi:[10.1109/36.934090](https://doi.org/10.1109/36.934090).
- Soh, L.-K., and C. Tsatsoulis. 1999. "Texture Analysis of SAR Sea Ice Imagery Using Gray Level Co-occurrence Matrices." *IEEE Transactions on Geoscience and Remote Sensing* 37 (2): 780–795. doi:[10.1109/36.752194](https://doi.org/10.1109/36.752194).
- Soh, L.-K., C. Tsatsoulis, C. Bertoia, and D. Gineris. 2004. "ARKTOS: An Intelligent System for SAR Sea Ice Image Classification." *IEEE Transactions on Geoscience and Remote Sensing* 42 (1): 229–248. doi:[10.1109/TGRS.2003.817819](https://doi.org/10.1109/TGRS.2003.817819).
- Solberg, S., R. Astrup, J. Breidenbach, B. Nilsen, and D. Weydahl. 2013. "Monitoring Spruce Volume and Biomass with InSAR Data from TanDEM-X." *Remote Sensing of Environment* 139: 60–67. doi:[10.1016/j.rse.2013.07.036](https://doi.org/10.1016/j.rse.2013.07.036).

- Solberg, S., D. J. Weydahl, and R. Astrup. 2015. "Temporal Stability of X-Band Single-Pass InSAR Heights in a Spruce Forest: Effects of Acquisition Properties and Season." *IEEE Transactions on Geoscience and Remote Sensing* 53 (3): 1607–1614. doi:10.1109/TGRS.2014.2346473.
- Stroeve, J., M. M. Holland, W. Meier, T. Scambos, and M. Serreze. 2007. "Arctic Sea Ice Decline: Faster than Forecast." *The Cryosphere* 34 (9): L09501. doi:10.1029/2007GL029703.
- Stumpf, A., and N. Kerle. 2011. "Object-oriented Mapping of Landslides Using Random Forests." *Remote Sensing of Environment* 115 (10): 2564–2577. doi:10.1016/j.rse.2011.05.013.
- Vachon, P. W., F. M. Monaldo, B. Holt, and S. Lehner. 2004. *SAR Marine User's Manual: Ocean Surface Waves and Spectra*. C. R. Jackson and J. R. Apel. Eds.. Washington, DC, USA:NOAA NESDIS Office of Research and Applications.2004. 139–169.
- Vapnik, V. 1995. *The Nature of Statistical Learning Theory*. New York: Springer-Verla.
- Zakhvatkina, N. Y., V. Y. Alexandrov, O. M. Johannessen, S. Sandven, and I. Y. Frolov. 2013. "Classification of Sea Ice Types in ENVISAT Synthetic Aperture Radar Images." *IEEE Transactions on Geoscience and Remote Sensing* 51 (5): 2587–2600. doi:10.1109/TGRS.2012.2212445.
- Zakhvatkina, N. Y., A. Korosov, S. Muckenhuber, S. Sandven, and M. Babiker. 2017. "Operational Algorithm for Ice-water Classification on Dual-polarized RADARSAT-2 Images." *Cryosphere* 11 (1): 33–46. doi:10.5194/tc-11-33-2017.